XMM-Newton衛星で探るSS433のジェット周辺のプラズマ構造

久保田 香織

卒業論文

東京工業大学 理学部 物理学科

2005年 3月

The Plasma Structure in the Vicinity of the Jet of SS433 with XMM-Newton

Kaori Kubota

Graduate Thesis

Submitted to the Department of Physics, the School of Science,

Tokyo Institute of Technology

March 2005

Abstract

SS433 is an enigmatic X-ray binary with a precessing, relativistic bipolar jet. Although it has been studied for more than 25 years since its discovery, its fundamental properties, such as the origin of the jet's acceleration , collimation, and precession, and the nature of the compact object, are not resolved.

X-ray observations are the best means to explore the core of system. In this thesis the observation data of SS433 taken with the pn camera of the European Photon Imaging Camera (EPIC) onboard XMM-Newton on 2003 October 18 and 2003 October 25 are analyzed. An Fe K-shell absorption edge at E$\simeq$7.9 keV (it is different from that of neutral atom at rest frame) with a column density of $N_{\rm H} \simeq 10^{24}\,{\rm cm}^{-2}$ is detected in the 5.0$-$10 keV range spectra. Two mechanisms to explain the edge-energy shift are proposed: 1. The Fe ion in the absorbing plasma is considerably ionized as $\rm Fe\,_{XV} - Fe\,_{XVIII}$. 2. The attenuating matter is moving along the blue-shifted jet.

In the former model, the estimated size of the absorbing plasma would be much smaller than the X-ray jet and would not cover it, unless the plasma is photoionized by hidden X rays which is not visible from us. A promising candidate for the hidden X rays are the emission from the inner accretion disk and the base of the jets .

An absorbing matter moving along the blue-shifted jet may be explained in terms of an internal structure of the jet or dense blobs around the jet.

Contents

Chapter 1

Introduction

Today about 20 "microquasers", X-ray binaries consisting of a compact object (a black hole or a neutron star), an accretion disk, and one relativistic jet or two, are known in our Galaxy (Mirabel and Rodíguez 1999). SS433 is a strange source even among those "microquasers" for its puzzling features: an extremely stable continuous bipolar jet emanating at a quarter of the speed of light, so called "moving" emission lines in the spectrum due to the precession of the jet axis with a precessional period of ~ 162 days. SS433 has many problems which are still unsolved: jet formation mechanism, precession mechanism and the nature of the compact object; whether a black hole or a neutron star.

X-ray observations are the best means to explore the nature, because X rays provide information about the core of the system and the base of jets. Since SS433 is identified as the X-ray source A1909+04, it has been observed with most of X-ray missions. Recent studies with *ASCA* (1993−2001) and *Chandra X-ray Observatory* (1999−) have focused out the emission lines in the spectrum. But the X-ray continuum has hardly been examined.

Thanks to the very large effective area of the *XMM-Newton*, we can get statistically excellent data. In particular, the EPIC-pn onboard *XMM-Newton* has a good sensitivity around iron lines ($5.0-10\,\mathrm{keV}$). In this thesis, I use the $5.0-10\,\mathrm{keV}$ data of *XMM-Newton* EPIC-pn for a careful study the continuum of SS433.

In this chapter, I present the basic data of the system and highlighten some X-ray observations. For more detailed review, see e.g., Margon (1984).

1.1 Basic data of SS433

SS433 is the 433rd star in the "SS catalogue" (Stephenson and Sanduleak 1977). SS433 is located near the galactic plane, l=39.7°, b=−2.2° (Margon 1984) and is identified as the

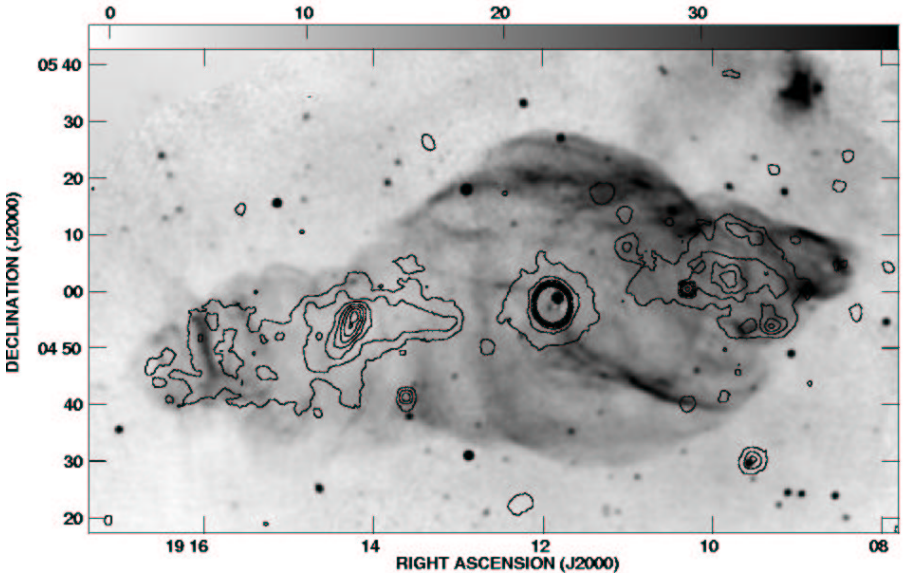

Figure 1.1: VLA continuum mosaic of W50 at 1.5 GHz (Dubner *et al.* 1998) and *ROSAT* X-ray contour at $0.2 - 2.4$ keV (Brinkmann *et al.* 1996). The counterpart of SS433 is the bright unresolved source at the center of the image. The lateral E−W extension is caused by the injection of the jets from SS433.

X-ray source A1909+04 (Seaquist *et al.* 1978). The position of SS433 is near the center of the supernova remnant W50 (Figure 1.1). SS433 is a galactic object and the distance to SS433 is estimated as about 4.85 kpc (Vermeulen *et al.* 1993).

Figure 1.2 shows the temporal optical spectra of SS433 on 1978. Two "moving" emission features are seen at $\sim$ 6100 $\mathring{A}$ and $\sim$ 7400 $\mathring{A}$. The motion can be explained by Doppler variation with a changing radial velocity of the emitting matter. Figure 1.3 shows the time variation of Doppler shifts of the "moving" emission features. An almost-164-days period is seen.

Changing of the Doppler shifts can be explained by the *kinematic model* with five independent parameters. Geometry of the *kinematic model* is shown in Figure 1.4. The two oppositely directed jets precesses with a precessional period P_{prec} tracing a precession cone with an half opening angle θ. The precessional axis of the precession cone has an inclination angle i. The emission lines from approaching jet shift to blue. The emission line from receding jet shift to red. Margon and Anderson (1989) determined these parameters using the observations conducted over a decade. The parameters are shown in Table 1.1. In this thesis, the jet which approaches to us on average is defined as the "blue jet", and the other which recedes from us on average is defined as the "red jet".

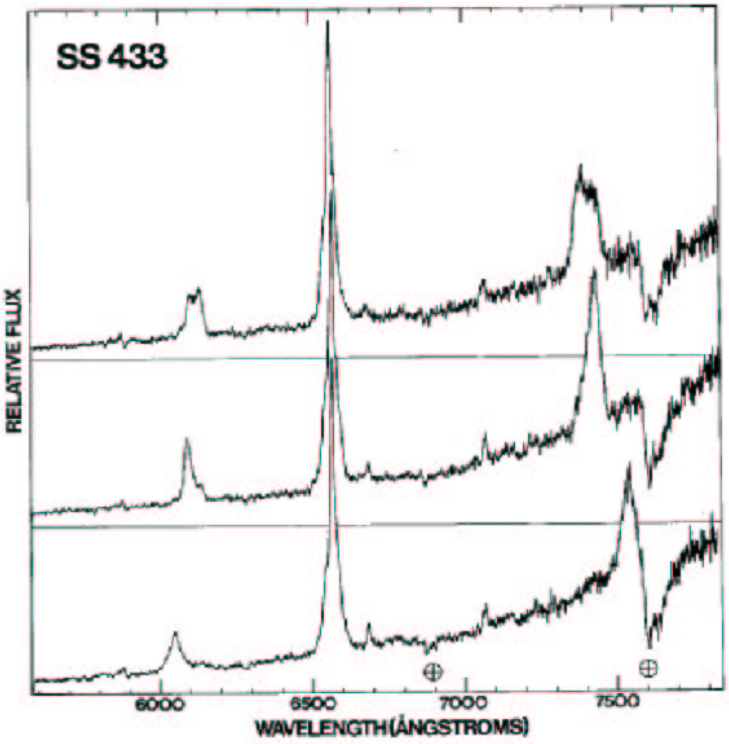

Figure 1.2: The red/infrared spectrum of SS433 around the Hα (6563 $\mathring{A}$) line. The changes in both wavelength and profile of two unidentified emission features at $\sim$ 6100 and $\sim$ 7400 $\mathring{A}$ are well-illustrated. He I λ 5876, 6678, and 7065 emission lines are visible. The telluric absorptions are indicated by $\oplus$. The top, middle, and bottom panels were observed on 1978 October 23, 24, and 26, respectively (Margon *et al.* 1979a).

Table 1.1: Best fit model parameters for SS433 (Margon and Anderson 1989). Parameter uncertainties quoted are $\pm 1\sigma$.

Parameter	Value	Note
t_0	43562.37 ± 0.30 (MJD[a])	Time at which precessional phase $\Psi(t)$ equals to zero[b].
v	0.2602 ± 0.0013	Velocity of the jet in unit of c.
$P_{\rm prec}$	162.50 ± 0.03 days	Precessional period.
θ	$19^\circ.85 \pm 0^\circ.17$	Half opening angle of the pression cone.
i	$78^\circ.83 \pm 0^\circ.10$	Inclination angle of the precessional axis.

a): Modified Julian Day. MJD is defined by an equation of Julian Day (JD)$-$2400000.5 days

b): There are two instants during a precessional period when the jets of SS433 are perpendicular to the line of sight. Margon and Anderson (1989) define the precessional phase Ψ so that these instants occur at $\Psi = 0$ and $\Psi = 0.316$.

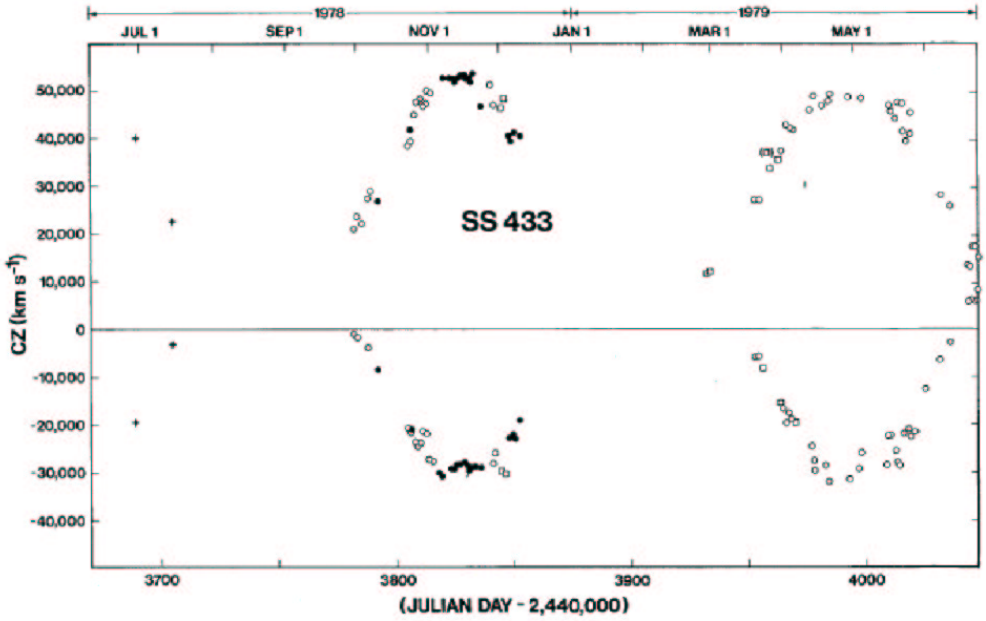

Figure 1.3: Doppler shift of the emission lines in SS433 versus time. Note that although the ordinate displays the Doppler shifts in units cz, the actual kinematic velocity values are somewhat different due to the significant Lorentz factor (Margon *et al.* 1979b).

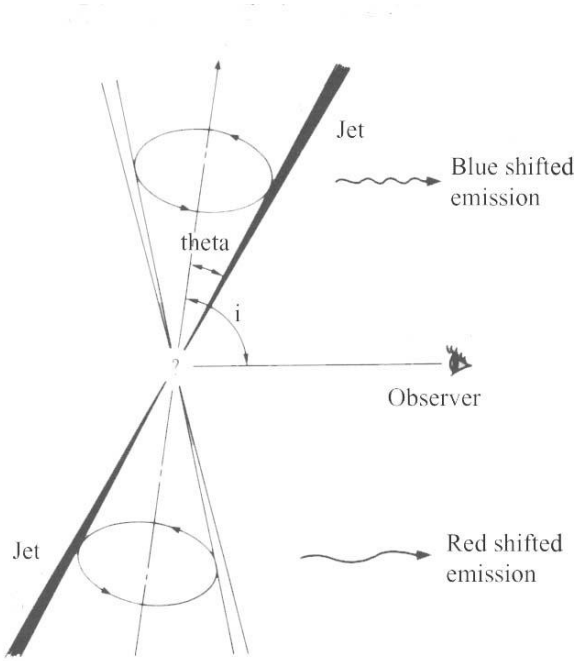

Figure 1.4: Geometry of the precessing jets of SS433 (福江 1993).

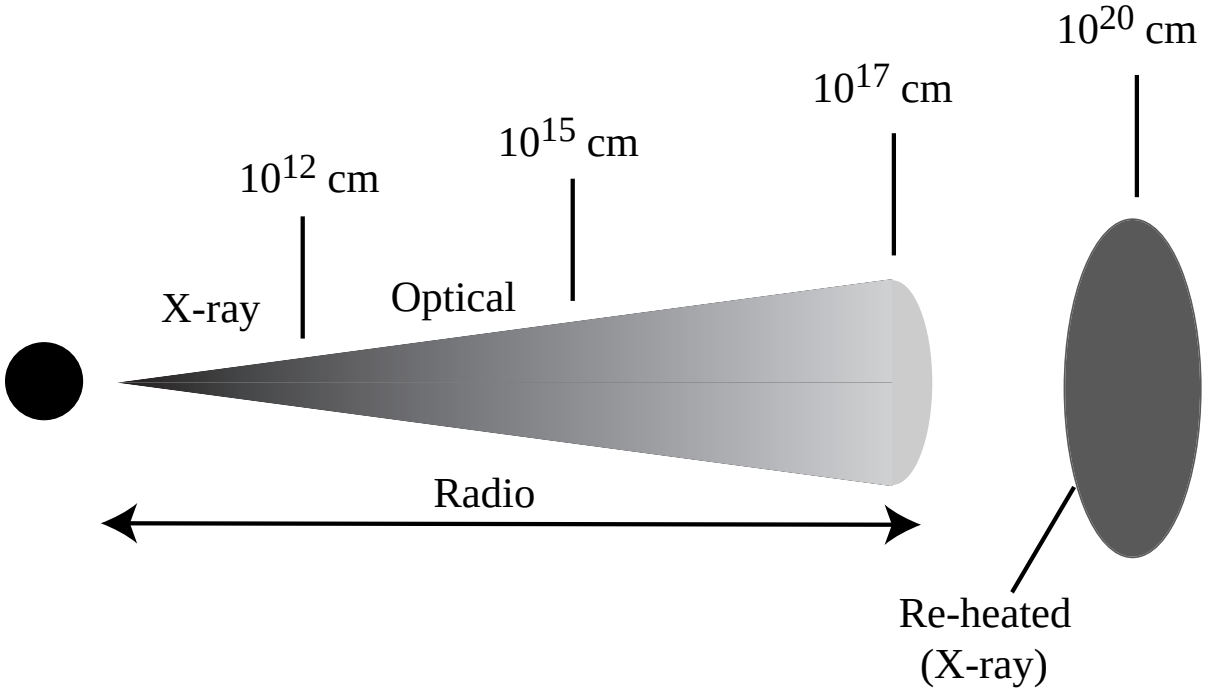

Figure 1.5: The typical scales of the jet of SS433.

SS433 is also an eclipsing binary system. SS433 consists of a compact object and a main-sequence companion star. Glagyshev *et al.* (1987) determined the orbital period $P_{\rm orb} = 13.0820 \pm 0.0007$ days.

1.2 The typical scales of SS433

The typical scales of the jet of SS433 is shown in Figure 1.5. The inner jet is with a scale of 10^{12} cm is observed in X rays. The $10^{12} - 10^{15}$ cm jet observed optically. The 10^{17} cm jet is observed in radio band. The re-heated area which radiates X rays resides at 10^{20} cm from the compact object. The radius of the accretion disk is as the same order as the lenght of the X-ray jet. The re-heated area is located on the lateral extension of W50.

1.3 X-ray observations of SS433

X-ray observations are necessary to probe the core of the system and the base of the jets. Since SS433 was identified by the X-ray source A1909+04, it is observed with most the X-ray satellites. In this section, I briefly review observations and findings with EXOSAT, Ginga, ASCA, Chandra and XMM-Newton.

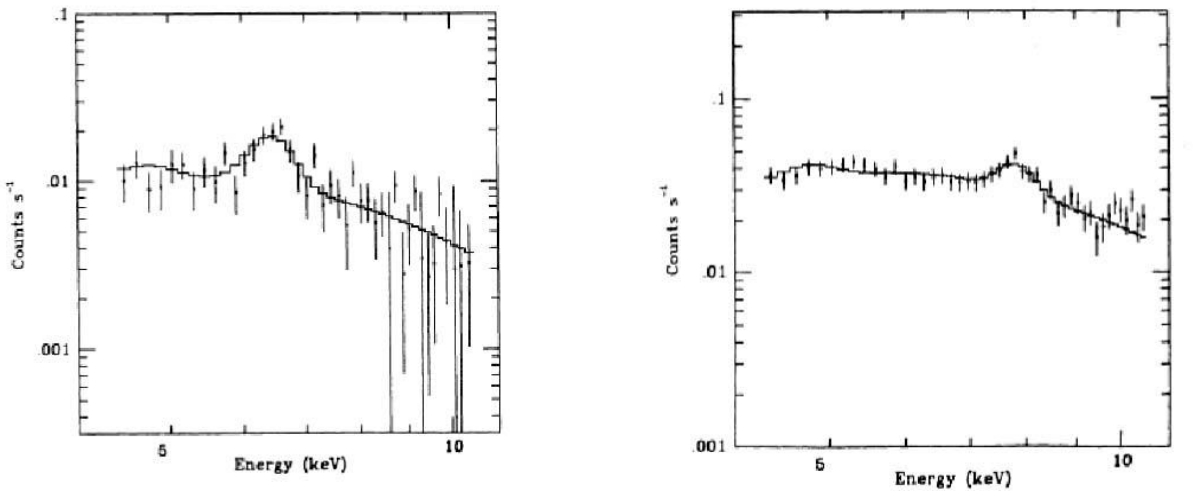

Figure 1.6: *EXOSAT* GSPC X-ray spectra of SS433 at two different precessional phase. The histogram show the best-fit spectra which consist of a thermal bremsstrahlung continuum plus an emission line. Error bars shown are of $\pm 1\sigma$ (Watson *et al.* 1986).

1.3.1 EXOSAT

In 1983−85, an emission line feature around $6 - 7\,\mathrm{keV}$ was detected with the *EXOSAT* GSPC. Watson *et al.* (1986) has interpreted the feature as the Doppler shifted Fe $_{\mathrm{XXV}}$ Kα emission line from the blue jet and showed that the line energy moves according to the predictions of Margon (1984). Watson *et al.* (1986) have reported that there is only one emission line seen in the spectra taken in *EXSOSAT*. They assumed that the blue jet is visible while the other jet is hidden behind the accretion disk. Based on this assumption, the jet was concluded to be shorter than the disk dimension of $\leq 10^{12}\,\mathrm{cm}$.

1.3.2 Ginga

In 1987−1989, the *Ginga* LAC observed SS433 several times. Thanks to the large effective area and high sensitivity to hard X-ray photons up to $\sim 30\,\mathrm{keV}$, detailed observation of SS433 in eclipse could be done by the *Ginga* LAC. From these observations, Kawai *et al.* (1989) have concluded that the X-ray jets is hidden by the companion star in eclipse. The X-ray spectral continuum is explained by a thermal bremsstrahlung continuum with $kT \leq 30\,\mathrm{keV}$ and $kT \sim 12\,\mathrm{keV}$, out of eclipse and eclipse, respectively. Brinkmann *et al.* (1991) have applied a hydrodynamical radiative plasma flow model to the jet and numerically calculated spectra to compare with the *Ginga* data. Two extreme types of

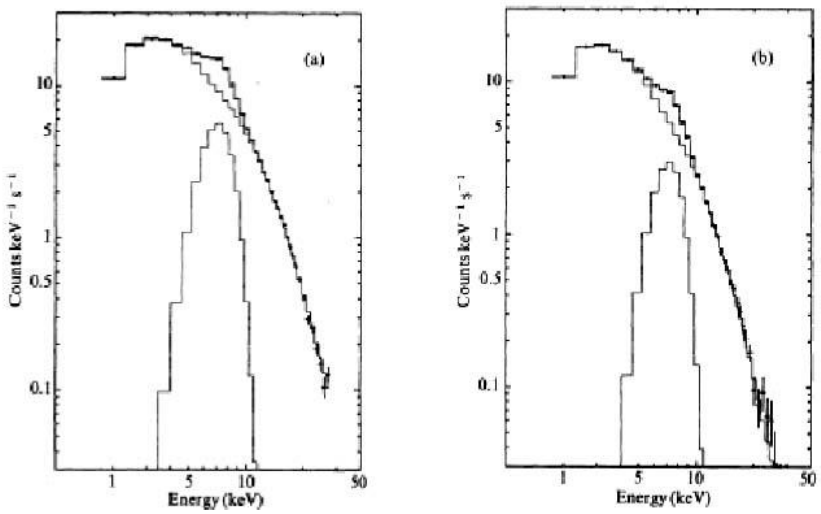

Figure 1.7: *Ginga* LAC spectra of SS433 at two different binary phases: (a) out of eclipse and (b) during eclipse. Histograms show a best-fit model and its components, including a thermal bremsstrahlung continuum and a broad Gaussian emission line at 7 keV (Kawai *et al.* 1989).

jet model have been assumed; a high density ($\sim 10^{13}\,\mathrm{cm}^{-3}$) thin jet ($\sim 10^{10}\,\mathrm{cm}$) and a low density ($\sim 10^{11}\,\mathrm{cm}^{-3}$) fat jet ($\sim 10^{12}\,\mathrm{cm}$). At that time, short jet model was believed to be realistic based on *EXOSAT*'s results.

1.3.3 ASCA

In 1993, a surprising spectrum (Figure 1.8) was shown by the *ASCA* SIS, using its high energy resolution. Many pairs of Doppler shifted emission lines, such as Si XIV, S XV, S XVI, Ar XVII, Ar XVIII, Ca XIX, Fe XXV, Fe XXVI and Ni XXVII, have been detected (Kotani *et al.* 1994). By the detection of emission lines from the red jet, the estimate of the lengh of the X-ray jets was vastly improved. Kotani *et al.* (1996) estimated the base of the jet temperature as $\sim 20\,\mathrm{keV}$, using the line flux raito of Fe XXVI Kα to Fe XXV Kα. Kotani (1998) suggested that the low energy emission lines from the receding jet are generally weaker than those from the approaching jet, and sometimes absent. This can be explained if an absorbing matter is present in the line of sight to the receding jet.

1.3.4 Chandra X-ray Observatory

Today, the *Chandra X-ray Observatory* HETGS has the highest energy resolution among X-ray missions currently orbiting. Marshall *et al.* (2002) have reported on the observa-

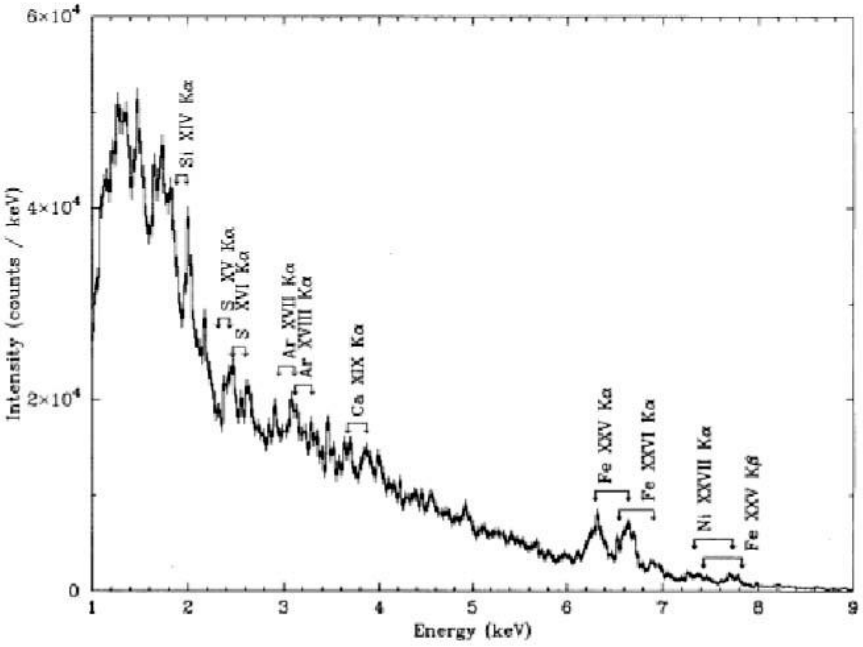

Figure 1.8: The X-ray count spectrum of SS433 obtained with *ASCA* SIS on 1993. Pair of Doppler shifted lines are identified (Kotani *et al.* 1994).

tions of SS433 in 1999, and obtained the value of line broadening as $1700\,\mathrm{km\,s^{-1}}$. They have estimated that the electron density is $10^{14}\,\mathrm{cm^{-3}}$ and the gas temperature $1.3\times10^{7}\,\mathrm{K}$, using the density-sensitive Si $_{\mathrm{XIII}}$ triplet. Namiki *et al.* (2003) have reported on the observation of 2001, and have estimated the initial temperature of the jets to be $\sim 20\,\mathrm{keV}$. They obtained that the widths of the Fe $_{\mathrm{XXV}}$ Kα and Si $_{\mathrm{XIII}}$ Kα lines correspond to velocity dispersions of $2100\,\mathrm{km\,s^{-1}}$ and $840\,\mathrm{km\,s^{-1}}$, respectively. This can be explained if the jets are collimated in the range of the X-ray jet.

1.3.5 XMM-Newton

The *XMM-Newton* has the largest effective area in the current missions. Brinkmann *et al.* (2005) have reported on a *XMM-Newton* EPIC spectra analysis on 2003. They ruled out the simple continuum model used previously. They made a jet model in terms of thermal emissions from conically out-flowing jets and estimate the temprature at the base of the jets as $\sim 17\,\mathrm{keV}$ and the density $\sim 10^{12}\,\mathrm{cm^{-3}}$.

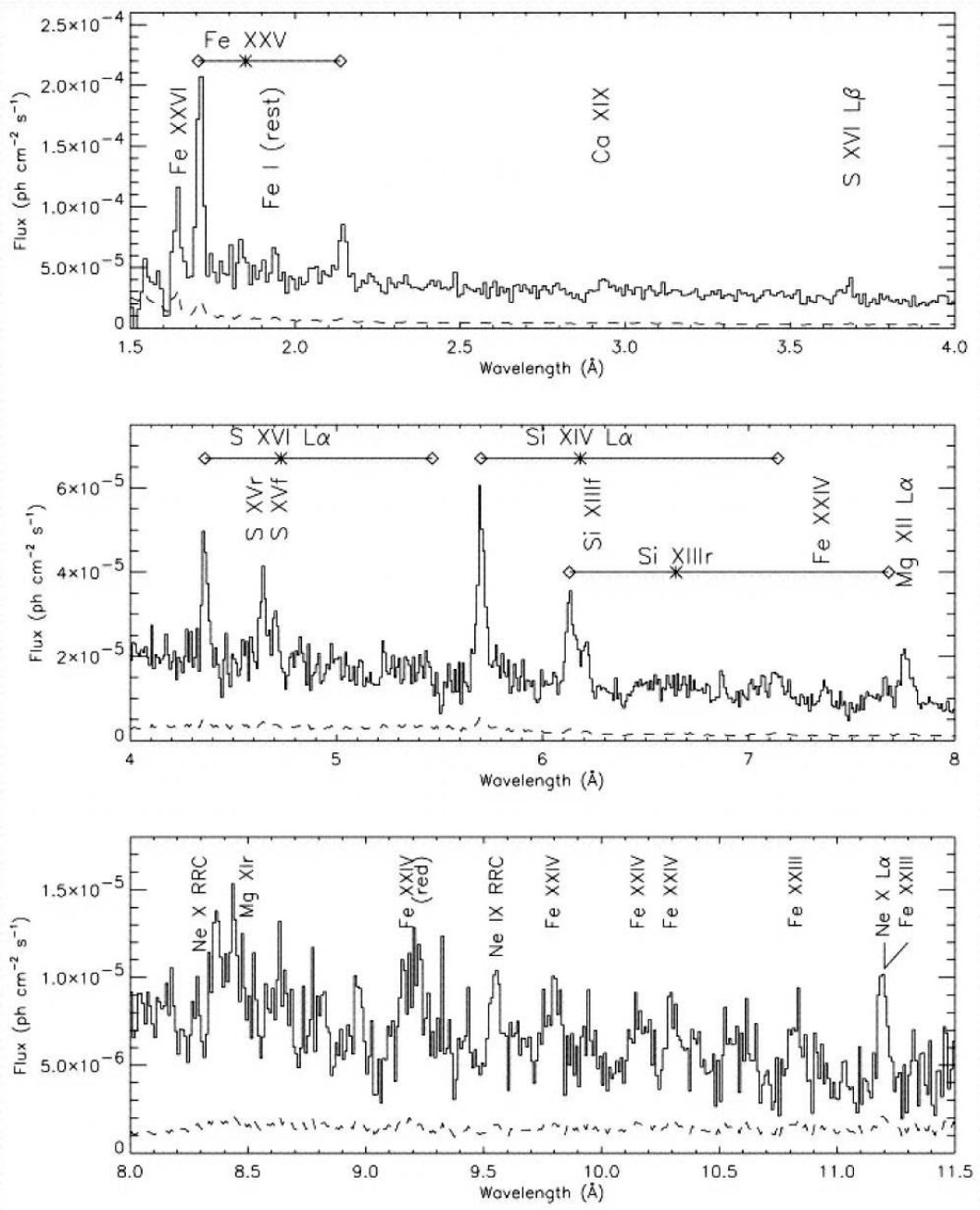

Figure 1.9: The X-ray spectrum of SS433 observed with the *Chandra* HETGS. All lines originate in the blue jet unless shown otherwise. Horizontal lines connect the locations of the pair of Doppler shifted lines (*diamonds*) to the rest wavelengths (*asterisks*). The dashed lines gives the statistical uncertainties (Marshall *et al.* 2002).

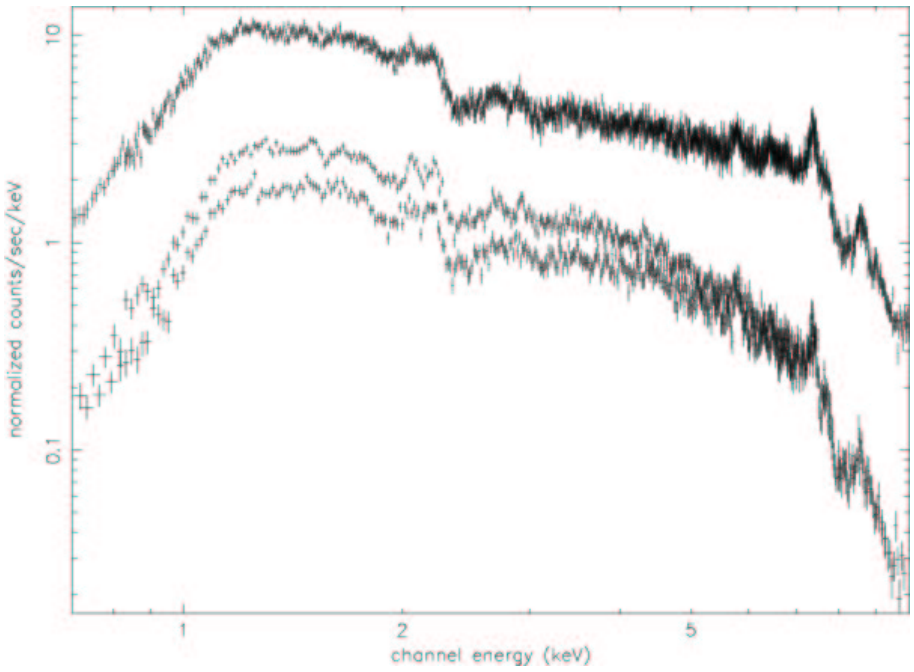

Figure 1.10: The X-ray spectra of SS433 observed with *XMM-Newton* EPIC; *top*: pn data, *middle*: MOS-1 data (timing mode), and *bottom*: MOS-2 data (full window mode) (Brinkmann *et al.* 2005).

Chapter 2

Instrumentation

The observations were carried out with the *XMM-Newton*. In this chapter, the *XMM-Newton* and the EPIC camera are briefly described. For more details, see *XMM-Newton* Users' Handbook (Ehle *et al.* 2004).

2.1 XMM-Newton

The *XMM-Newton* is the second of ESA[1] 's four "cornerstone" missions. It was launched on 1999 December 10 and carries two types of telescope; three Wolter type-1 X-ray telescopes, with different X-ray detectors in their foci, and a 30-cm optical/UV telescope with a microchannel-plate pre-amplified CCD detector in its focal plane. Thus, the *XMM-Newton* offers simultaneous access to two windows of the electromagnetic spectrum; X-ray and optical/UV.

The *XMM-Newton* provides the following three types of science instrument:

1. European Photon Imaging Camera (EPIC)
   3 CCD cameras for X-ray imaging, moderate resolution spectroscopy, and X-ray photometry; the two different types of EPIC camera, MOS and pn, are described in §2.2. The *XMM-Newton* carries 2 MOS cameras and one pn.

2. Reflection Grating Spectrometer (RGS)
   2 essentially identical spectrometers for high-resolution X-ray spectroscopy and spectro-photometry.

3. Optical Monitor (OM)
   for optical/UV imaging and grism spectroscopy.

[1] European Space Agency

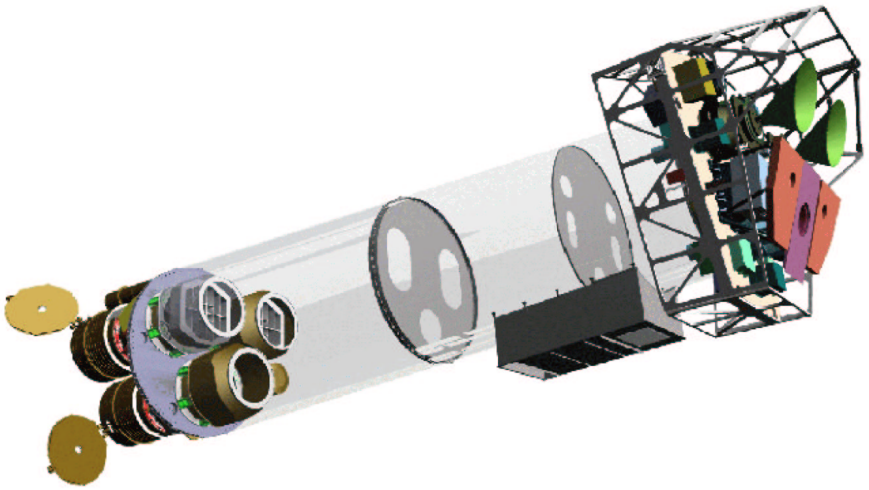

Figure 2.1: Sketch of the *XMM-Newton* payload. The mirror modules, two of which are equipped with Reflection Grating Arrays, are visible at the lower left. At the right end of the assembly, the focal X-ray instruments are shown: The EPIC MOS cameras with their radiators (black/green "horns"), the radiator of the EPIC pn camera (violet) and those of the (light blue) RGS detectors (in pink). The OM telescope is obscured by the lower mirror module.

The three EPIC cameras and the two detectors of the RGS spectrometers reside in the focal planes of the X-ray telescopes, while the OM has its own telescope. A sketch of the *XMM-Newton* payload is displayed in Figure 2.1. There are in total six science instruments on board the *XMM-Newton*, which are operated simultaneously (unless prohibited by constraints, for example, excessive target brightness). The instruments can be operated independently and each in different modes of data acquisition. Observers will receive data from all science instruments.

The most important characteristics of the *XMM-Newton* are compiled in Table 2.1. The basic characteristics of the *XMM-Newton* are:

- Simultaneous operation of all science instruments
  If not prohibited, e.g. by target brightness constraints, all six *XMM-Newton* science instruments operate simultaneously. They work independently (i.e., exposures of the individual instruments do not necessarily start and end at the same time).

- High sensitivity
  The *XMM-Newton* carries the X-ray telescopes with the largest effective area of a focusing telescope ever: the total mirror geometric effective area at 1.5 keV energy is about 1550 cm^2 for each telescope, *i.e.*, 4650 cm^2 in total.

- Good angular resolution
  XMM-Newton's high sensitivity is achieved by using 58 thin nested mirror shells in each X-ray telescope. The achieved point-spread function (PSF) has a full width at half maximum (FWHM) on the order of 6″ and a HEW, at which 50% of the total energy are encircled, of about 15″.

- Moderate and high spectral resolution
  The EPIC CCD cameras have moderate spectral resolution (with a resolving power, E/ΔE, of about 20−50). The RGS spectrometers offer much higher spectral resolution, with a resolving power in the range of 200−800.

- Simultaneous optical/UV observations
  Observations with the co-aligned OM optical/UV telescope render possible the monitoring and identification of optical/UV counterparts of X-ray sources seen by the X-ray telescopes as well as imaging of the surrounding field.

- Long continuous target visibility
  A highly elliptical orbit offers continuous target visibility of up to about 40 hours, with a minimum height for science observations of 46,000 km. This is very favorable for studies of source variability and also in order to achieve a high overall observatory efficiency.

2.2 European Photon Imaging Camera

Two of *XMM-Newton*'s X-ray telescopes are equipped with EPIC MOS (Metal Oxide Semi-conductor) CCD arrays, the third carries a different CCD camera called EPIC pn. In a nutshell, the *XMM-Newton* EPIC cameras offer the possibility to perform extremely sensitive imaging observations over a field of view of 30′ and the energy range from 0.15 to 15 keV, with moderate spectral ($E/\Delta E \sim 20-50$) and angular resolution (6″ FWHM; 15″ HEW). The pn type camera can be operated with a very high time resolution down to 0.03 ms in the timing mode and 0.007 ms (but with a very low duty cycle of 3%) in the burst mode. Note however that the absolute timing accuracy is determined by the process which correlates the on-board time to the universal time.

Table 2.1: XMM-Newton characteristics

Instrument	EPIC MOS	EPIC pn	RGS	OM
Bandpass	0.15−12 keV	0.15−15 keV	0.35−2.5 keV	180−600 nm
Orbital target vis.[1]	5−135 ks	5−135 ks	5−145 ks	5−145 ks
Sensitivity[2]	$\sim 10^{-14}$ [3]	$\sim 10^{-14}$ [3]	$\sim 8\times10^{-5}$ [4]	20.7 mag [5]
Field of view (FOV)	$30'$	$30'$	$\sim 5'$	$17'$
PSF (FWHM/HEW)	$5''/14''$	$6''/15''$	N/A	$1.4'' - 1.9''$
Pixel size	40 μm ($1.1''$)	150 μm ($4.1''$)	81 μm ($9\times10^{-3}\AA$)	$0.476513''$
Timing resolution[6]	1.5 ms	0.03 ms	16 ms	0.5 s
Spectral resolution[7]	$\sim$70 eV	$\sim$80 eV	0.04/0.025 $\AA$[8]	350 [9]

1): Total time available for science per orbit; minimum of 5 ks in order to ensure observatory efficiency. XMM-Newton science observations can only be performed outside the Earth's radiation belts.

2): With an exposure time of 10 ks.

3): In the range 0.15−15.0 keV, in units of erg s^{-1} cm^{-2}.

4): O VII 0.57 keV line flux in photons cm^{-2} s^{-1}, for an integration time of 10 ks and a background of 10^{-4} photons cm^{-2} s^{-1} keV^{-1}.

5): 5-σ detection of an A0 star in 1000 s.

6): In fast data acquisition mode (*i.e.*, fast mode for OM and timing mode for EPIC, high time resolution mode for RGS, reading out only one of nine CCDs).

7): At 1 keV energy. At the energy of Fe Kα (6.4 keV), the energy resolution of both EPIC cameras is about 150 eV.

8): In -1. and -2. order, resp.; at 1 keV, this corresponds to 3.2/2.0 eV (HEW).

9): Resolving power ($\lambda/\Delta\lambda$) with UV and optical grism.

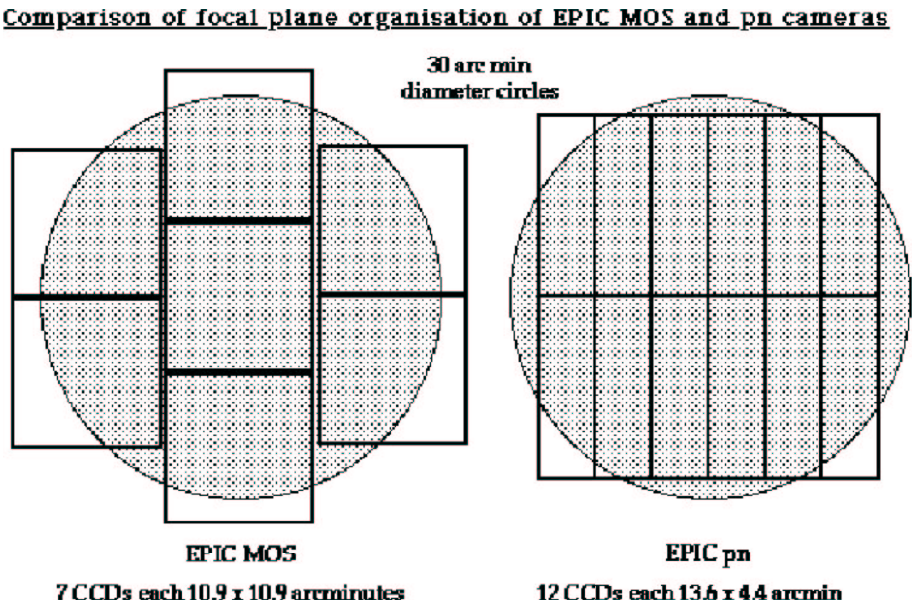

Figure 2.2: A rough sketch of the field of view of the two types of EPIC camera; MOS (left) and pn (right). The shaded circle depicts a 30′ diameter area. The MOS chip arrays consist of 7 individual identical, front-illuminated chips. The heart of the pn camera is a single Silicon wafer with 12 CCD chips integrated.

The detector layout and the baffled X-ray telescope FOV of both types of EPIC camera are shown in Figure 2.2. For all cameras the sensitive area of the detector is about 30′ across.

All EPIC CCDs operate in photon counting mode with a fixed, mode dependent frame read-out frequency, producing event lists. This allows for simultaneous imaging and non-dispersive spectroscopy due to the intrinsic energy resolution of the pixels.

2.2.1 Two types of EPIC camera; MOS and pn

The two types of EPIC camera are fundamentally different. This does not only hold for the geometry of the MOS chip array and the pn chip array (Figure 2.2), but other properties as well, like *e.g.*, their readout times. The readout of the pn chips is much faster than that of the MOS cameras, because each pixel column has its own readout node. Another important difference is that the MOS chips are front-illuminated, while the pn CCDs are back-illuminated, which affects the detector quantum efficiencies decisively (§2.2.4).

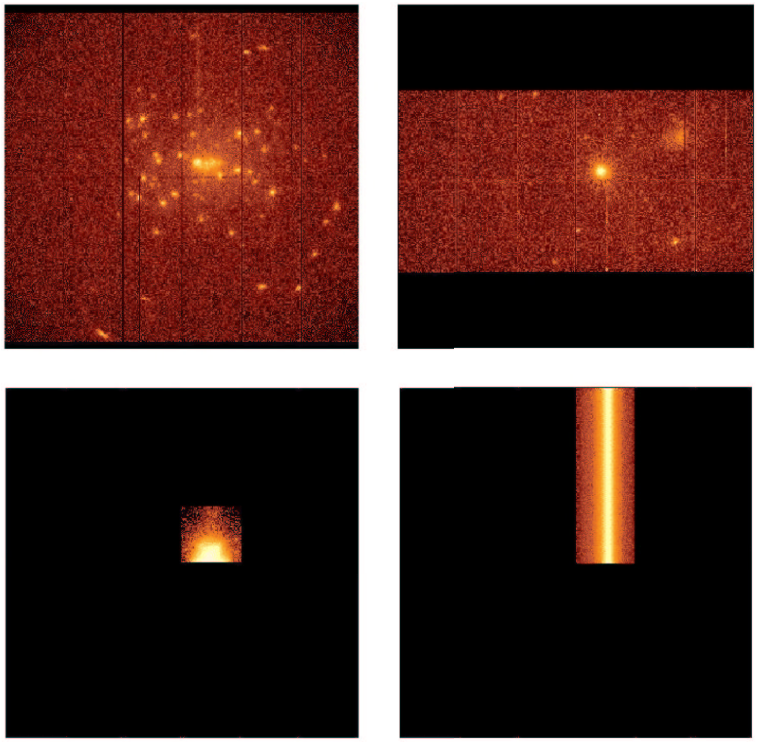

Figure 2.3: Operating modes for thae pn-CCD camera: top left: Full frame and extended full frame mode, top right: Large window mode, bottom left: Small window mode and bottom right: Timing mode. The burst mode is different from the timing mode as the source position is not read out, *i.e.* rows 181-200 will be dark.

2.2.2 Science modes of the EPIC cameras

The EPIC cameras allow several modes of data acquisition. Note that in the case of MOS the outer ring of 6 CCDs remain in standard imaging mode while the central MOS CCD can be operated separately. Thus all CCDs are gathering data at all times, independent of the choice of operating mode. The pn camera CCDs can be operated in common modes in all quadrants for full frame, extended full frame and large window mode, or just with one single CCD (CCD number 4) for small window, timing and burst mode.

The most important characteristics of the EPIC science modes (time resolution and count rate capability) are tabulated in Table 2.2. The active CCD areas for the different pn and MOS readout modes are shown in Figure 2.3 and Figure 2.4, respectively.

Table 2.2: Basic numbers for the science modes of EPIC

MOS (central CCD; pixels) 1 pixel = 1.1"	Time res olution	Live time[1] [%]	Max. count rate[2] diffuse[3] (total) [s^{-1}]	Max. count rate[2] (flux) point source [s^{-1}] ([mCrab][4])
Full frame (600×600)	2.6 s	100.0	150	0.70 (0.24)
Large window (300×300)	0.9 s	99.5	110	1.8 (0.6)
Small window (100×100)	0.3 s	97.5	37	5 (1.7)
Timing uncompressed (100×600)	1.5 ms	100.0	N/A	100 (35)
pn (array or 1 CCD; pixels) 1 pixel = 4.1"	**Time res olution**	**Live time[1] [%]**	**Max. count rate[2] diffuse[3] (total) [s^{-1}]**	**Max. count rate[2] (flux) point source [s^{-1}] ([mCrab][4])**
Full frame (376×384)	73.4 ms	99.9	1000(total)	8 (0.9)
Extended full frame[5] (378×384)	200 ms	100.0	370	3 (0.39)
Large window (198×384)	48 ms	94.9	1500	12 (1.3)
Small window (63×64)	6 ms	71.0	12000	130 (14)
Timing (64×200)	0.03 ms	99.5	N/A	1500 (160)
Burst (64×180)	7 μs	3.0	N/A	60000 (6300)

1): Ratio between the time interval during which the CCD is collecting X-ray events and the frame time.

2): "Maximum" to avoid deteriorated response due to photon pile-up. For the MOS cameras the maximum count rates are about 150 counts/s for full window and partial window imaging modes and 300 counts/s for timing mode. The pn telemetry limit is approx. 400 counts/s for the imaging modes and approx. 300 counts/s for the timing mode.

3): Values are representative of bright objects that are extended on scales much larger than the PSF core.

4): 1 mCrab = 2.4×10^{-11} erg s^{-1} cm^{-2} (in the energy range 2-10 keV).

5): 'Extended" means that the image collection time (*i.e.* the frame time) is longer than in the normal full frame mode.

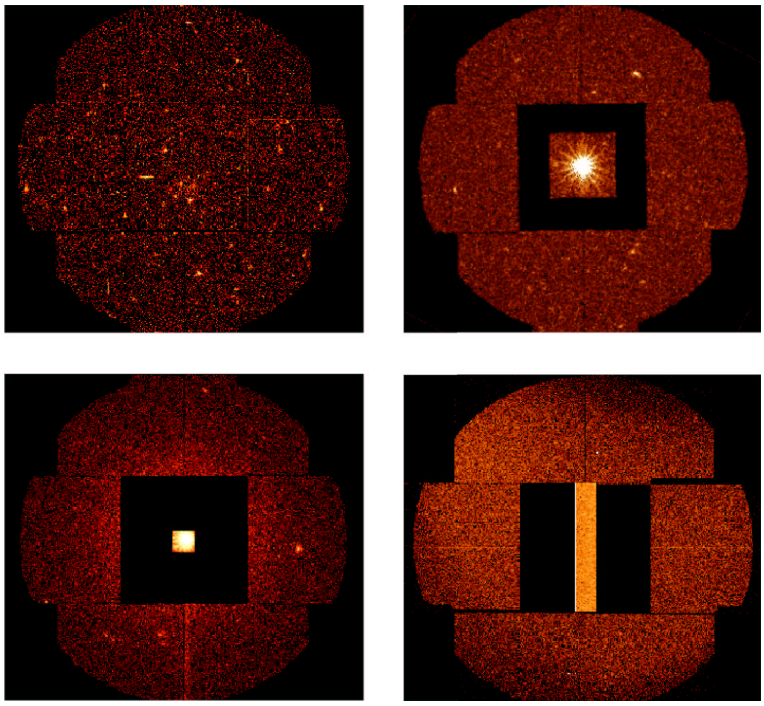

Figure 2.4: Operating modes for the MOS-CCD cameras: top left: Full frame mode, top right: Large window mode, bottom left: Small window mode and bottom right: Timing mode. In timing mode, the X axis of the central CCD is the projected image of the source, and has thus true spatial information; the Y axis does not carry any spatial information, but is a measure of time, with roll-over of 1024 time-units in the figure shown.

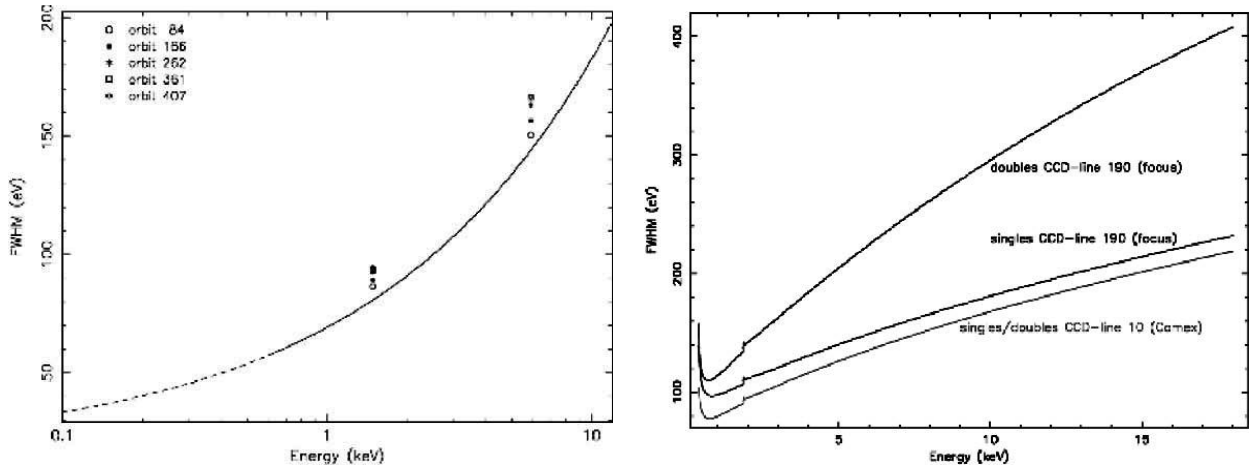

Figure 2.5: *left*: The EPIC MOS energy resolution (FWHM) as a function of energy. The solid curve is a best-fit $E^{0.5}$ function to ground calibration data between $0.1 - 12.0$ keV. Below around 0.6 keV (shown by the dotted region) surface charge loss effects distort the main photopeak significantly from a Gaussian form and, hence the effective energy resolution. Also plotted is the measured in-flight FWHM of the Al Kα (1.487 keV) and Mn Kα (5.893 keV) lines (using an extraction radius of 130 arcsec). *right*: The EPIC pn energy resolution (FWHM) as a function of energy. Curves are given for singles and double events (full frame mode) at the focus position as well as at a position 10 pixels away from the readout node.

2.2.3 Intrinsic energy resolution of EPIC

The CCD pixels of the EPIC cameras are energy sensitive, enabling non-dispersive spectroscopy. The resolving power of these cameras is determined by the intrinsic energy resolution of the individual pixels. The spectral resolution for a point source located at the nominal pointing position of both the EPIC MOS and pn CCDs, as a function of energy, is displayed in Figure 2.5. Also plotted in Figure 2.5 (left) are the measured in-flight FWHM of the Al Kα and Mn Kα on-board calibration lines, obtained in five different orbits. This shows a degradation of approximately 13% in the energy resolution of the MOS since the launch of XMM-Newton. For the pn camera, no significant degradation of the FWHM has been found.

2.2.4 EPIC quantum efficiencies

One of the factors to be taken into account when determining the effective area of the EPIC cameras is their quantum efficiency (QE). The QE of both types of EPIC CCD chip

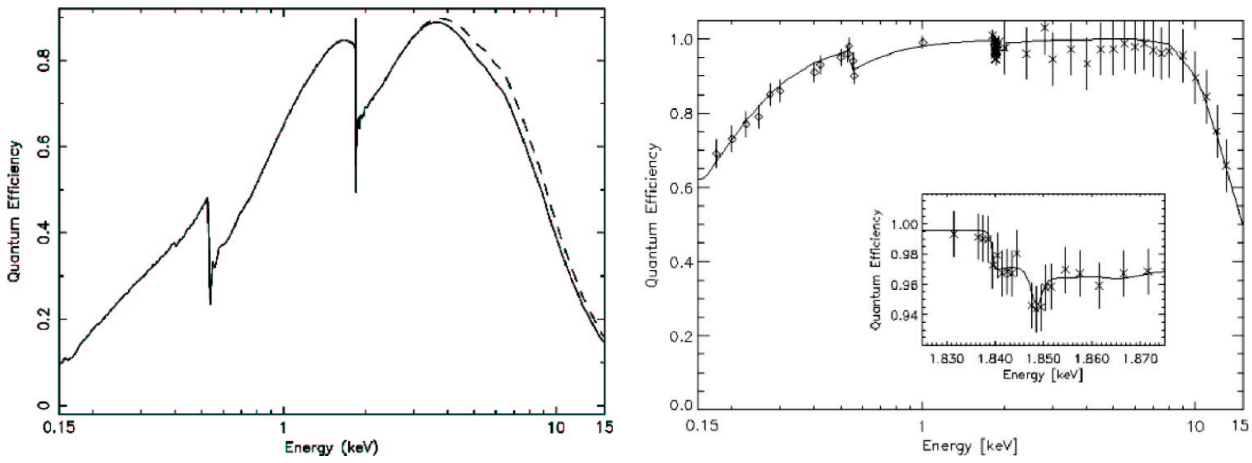

Figure 2.6: *left*: Quantum efficiency of the EPIC MOS1 (solid line) and MOS2 (dashed line) CCD1 chip as a function of photon energy. *right*: Quantum efficiency of the EPIC pn CCD chips as a function of photon energy (Strüder*et al.* 2001).

as a function of photon energy is displayed in Figure 2.6. It is the QE of the EPIC MOS chips that in practice limits the energy passband at its high end, while the pn camera can detect photons with high efficiency up to 15 keV. The event selection strategies can be important in modifying the overall detection efficiency.

2.2.5 EPIC filters and effective area

The next factor influencing the EPIC effective area, specifically in the low energy part of the passband, is the choice of the optical blocking filter. These filters are used, because the EPIC CCDs are not only sensitive to X-ray photons, but also to IR, visible and UV light. Each EPIC camera is equipped with a set of three separate filters, named thick, medium and thin. It is necessary for the observer to select the filter which maximises the scientific return, by choosing the optimum optical blocking required for the target of interest.

- Thick filter

  This filter should be used if the expected visible brightness of the target would degrade the energy scale and resolution of EPIC. It should be able to suppress efficiently the optical contamination for all point source targets up to m_V of $1-4$ (MOS) or m_V of $-2-1$ (pn). The range depends on the spectral type, with only extremely red (M stars for example) or blue colours causing the change to 3 magnitudes fainter level.

- Medium filter

  The optical blocking is expected to be about 10^3 less efficient than the thick filter, so it is expected that this filter will be useful for preventing optical contamination from point sources as bright as $m_V = 6 - 9$.

- Thin filter

  The optical blocking is expected to be about 10^5 less efficient than the thick filter, so the use of this filter will be limited to point sources with optical magnitudes about 12 magnitudes fainter than the corresponding thick filter limitations.

Figure 2.7 display the impact of the different filters on the soft X-ray response of both types of EPIC camera.

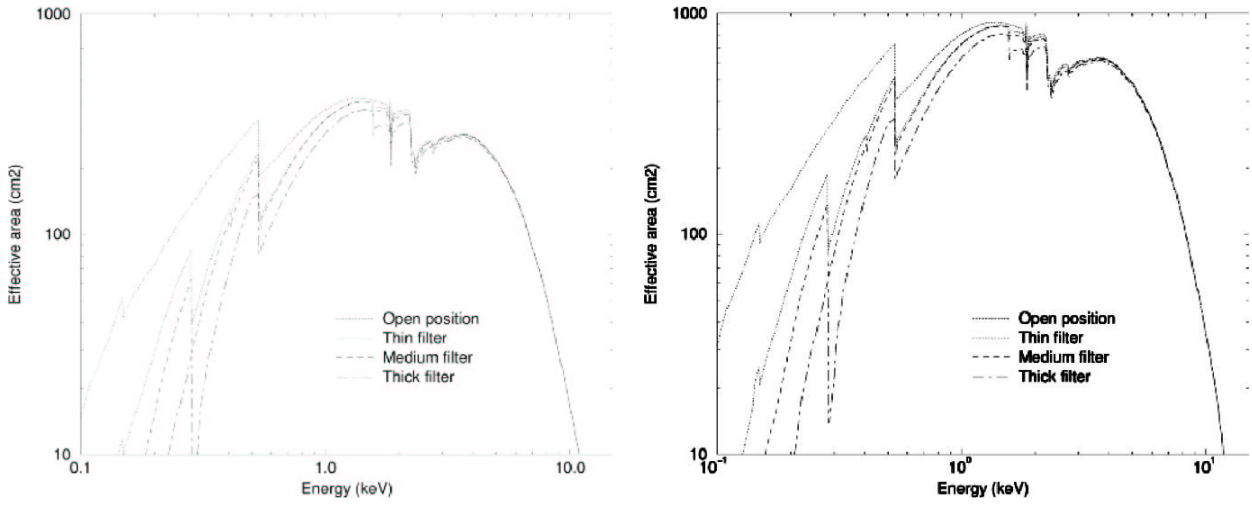

Figure 2.7: *left*: The EPIC MOS effective area for each of the optical blocking filters and without a filter. *right*: The EPIC pn effective area for each of the optical blocking filters and without a filter.

Chapter 3

The observation

Table 3.2 is the log of the observations of SS433 with XMM-Newton EPIC camera (until 2005 February). In all of the observations, the EPIC-pn camera was operated in Small Window mode, the EPIC-MOS1 camera was operated in Timing Mode, and the EPIC-MOS2 camera was operated in Full Window mode. The medium filters was used for the three cameras.

The observations on 2003 October 19, 2003 October 25, and 2004 April 15 affected by high radiation (*e.g.* the sun flare). SS433 states in the observations on 2003 April 2, 2004 March 20 and 2004 April 15 are in eclipse. The value of orbital phase, precession phase, and Doppler shifts of the red and the blue jet are calculated from the ephemeris of Goranskii *et al.* (1998).

I use only EPIC-pn camera data from the 2003 October 19 and 2003 October 25, because these are low background and out of eclipse. The two jets of SS433 in this study is at almost maximum separation. The log of observation is shown in Table 3.1. The one of the principle investigator of the observations is W.Brinkmann. All data have reducted with the reduction software XMMSAS ver. 6.0 (Loiseau *et al.* 2004).

Table 3.1: Log of the SS433 observation with the EPIC-pn used in this study

Performed Date	Exposure (sec)	$z_{red}{}^a$	$z_{blue}{}^b$
2003/10/19	20464	0.1635	-0.0922
2003/10/25	11464	0.1512	-0.0799

a): Doppler shift of the red jet at the middle time of the observation (expected values).

b): Doppler shift of the blue jet at the middle time of the observation (expected values).

Table 3.2: Log of the SS433 observation with XMM-Newton EPIC

Time UT	Instrument	Exposure (ks)	Precessional Phase[a] Ψ	Orbital Phase[b] ϕ	Remark
2003 April 02	pn	7.66			eclipse
16:19−18:28	MOS1	0.14	0.8497 ± 0.0000	0.047 ± 0.003	
	MOS2	0.56			
2003 April 04	pn	12.1			
14:21−18:00	MOS1	5.50	0.8620 ± 0.0005	0.196 ± 0.006	
	MOS2	5.47			
2003 April 06	pn	6.29			
16:06−17:52	MOS1	5.41	0.8745 ± 0.0002	0.351 ± 0.003	
	MOS2	5.83			
2003 April 08	pn	12.1			
14:05−17:44	MOS1	12.7	0.8866 ± 0.0005	0.500 ± 0.006	
	MOS2	12.9			
2003 October 19	pn	20.5			low BG*
00:02−05:50	MOS1	20.4	0.0797 ± 0.0007	0.288 ± 0.009	
	MOS2	20.7			
2003 October 25	pn	11.5			low BG*
03:59−07:17	MOS1	11.4	0.1174 ± 0.0004	0.756 ± 0.005	
	MOS2	11.7			
2004 March 20	pn	14.4			eclipse
15:21−20:24	MOS1	13.4	0.0271 ± 0.0006	0.031 ± 0.008	
	MOS2	13.8			
2004 April 15	pn	15.5			eclipse
13:51−18:16	MOS1	15.4	0.1870 ± 0.0006	0.013 ± 0.007	low BG*
	MOS2	15.7			

a,*b*): calculated from Goranskii *et al.* (1998). Times which $\phi = 0$ is at totally eclipse. Times which $\Psi = 0$ is at maximum separation between the two jets.

∗): low background.

Chapter 4

Data analysis

4.1 Data reduction

In this section, the reduction and the extraction of the spectral file from the data of 2003 October 19 and 2003 October 25 are described. Both data sets have processed in the same way.

26×27 RAW pixels around SS433 have been refered as the source region, the same number of pixels far from SS433 on the detector chip have been utilized as background region. More than 90% of X-ray photons from SS433 are in this source region. Only single and double events with quality flag of 0 have been used (for details of the XMM instruments see Ehle *et al.* 2004). Data with a background count rate exceeding one count per second are discarded. Finally, the spectra have been binned to contain more than 100 photons per bin. After the data screening, the integration times of the October 19 and the October 25 observations are 13094 sec and 7759 sec, respectively.

4.2 Spectral fitting

XSPEC version 11.2.x (latest version is 11.3.x, Arnaud and Dorman 2003) has been used for the spectral fitting.

In Figure 4.1 and Figure 4.2, I show the EPIC-pn spectra in the $5.0 - 10$keV energy band, fitted with a spectral model. Figure 4.1 and Figure 4.2 are the spectra taken on October 19 and from October 25, respectively. The fitting model is as a function of energy E given as

$$
\begin{aligned}
e^{-\sigma(E)\,N_{\mathrm{H\,W50}}}\times \quad & [A_1 \times \mathrm{Bremss1}(kT) + \mathrm{Fe\,I\,K}\alpha_{z=0} \\
& +(\mathrm{Fe\,XXV\,K}\alpha + \mathrm{Fe\,XXVI\,K}\alpha + \mathrm{Ni\,XXVII\,K}\alpha + \mathrm{Fe\,XXV\,K}\beta + \mathrm{Fe\,XXVI\,K}\beta)_{z=z_{\mathrm{red}}} \\
& +(\mathrm{Fe\,XXV\,K}\alpha + \mathrm{Fe\,XXVI\,K}\alpha + \mathrm{Ni\,XXVII\,K}\alpha + \mathrm{Fe\,XXV\,K}\beta + \mathrm{Fe\,XXVI\,K}\beta)_{z=z_{\mathrm{blue}}} \\
& +e^{-\sigma(E,E_{\mathrm{Fe}})\,N_{\mathrm{H\,lea}}} \times A_2 \times \mathrm{Bremss2}(kT)].
\end{aligned}
\tag{4.1}
$$

$e^{-\sigma(E)\,N_{\mathrm{H\,W50}}}$ expresses an interstellar photo-electric absorption toward the source and $\sigma(E)$ is the photo-electric cross section at E and $N_{\mathrm{H\,W50}}$ is the equivalent hydrogen column density. Because SS433 is located near the center of the supernova remnant W50, all of the emissions from SS433 are considered to be absorbed according to the column density toward W50. So we fixed $N_{\mathrm{H\,W50}}$ at W50's value, $N_{\mathrm{H}} = 0.7 \times 10^{22}\mathrm{cm}^{-2}$ (Safi-Harb and Ögelman 1997). $e^{-\sigma(E,E_{\mathrm{Fe}})\,N_{\mathrm{H\,lea}}}$ is same as$e^{-\sigma(E)\,N_{\mathrm{H\,W50}}}$ but $N_{\mathrm{H\,lea}}$ and the Fe K-shell edge energy are free parameters. Bremss1(kT) and Bremss2(kT) is the model for a thermal bremsstrahlung continuum with a parameter of the plasma temperature. The plasma temperatures of the both thermal bremsstrahlung spectra assuming "leaky absorber" in which the attenuating matter is partly covering the source. The model includes eleven narrow Gaussian lines: Five pairs of Doppler-shifted lines from $\mathrm{Fe\,XXV\,K}\alpha$, $\mathrm{Fe\,XXVI\,K}\alpha$, $\mathrm{Ni\,XXVII\,K}\alpha$, $\mathrm{Fe\,XXV\,K}\beta$ and $\mathrm{Fe\,XXVI\,K}\beta$ in the two jets, and one stationary line of $\mathrm{Fe\,I\,K}\alpha$. The Doppler shifts of the red jet and blue jet are set free: the Doppler shifts are the same among all the lines belonging to the same jet. As initial Doppler shifts, the predicted values shown in Table 3.1 are used. The best fit parameters is given in Table 4.1 and Table 4.2.

In the both spectra, the emission lines from the stationary $\mathrm{Fe\,I\,K}\alpha$, from $\mathrm{Fe\,XXV\,K}\alpha$ and $\mathrm{Fe\,XXV\,K}\beta$ from the both jets, $\mathrm{Fe\,XXVI\,K}\alpha$ and $\mathrm{Fe\,XXVI\,K}\beta$ from the blue jet are seen. The blended lines of $\mathrm{Ni\,XXVII\,K}\alpha$ and $\mathrm{Fe\,XXV\,K}\beta$ from the both jets are resolved in the spectral fitting. $\mathrm{Fe\,XXVI\,K}\beta$ from the red jet can not be detected. $\mathrm{Fe\,XXVI\,K}\alpha$ is seen in the spectrum from October 19 only. The Doppler shifts of the jets calculated from the line energies show little difference from the predicted values shown in Table 3.1.

The leaky-absorbed thermal bremsstrahlung continuum model give a good representation of the continuum spectra. From Ginga observations, the temperature of the thermal bremsstrahlung component has been determined as $kT = 10 - 40\,\mathrm{keV}$ (Yuan *et al.* 1995). But my results suggest a temperature less than 10 keV. This difference can be explained as follow: The radiation from the jets is multi-temperature bremsstrahlung emission. However, a one-temperature bremsstrahlung model has been used to fit my data. The representative temperature is a function of the bandwidth of the detector, because the higher photon energies the detector can measure, the more dominant a spectral component

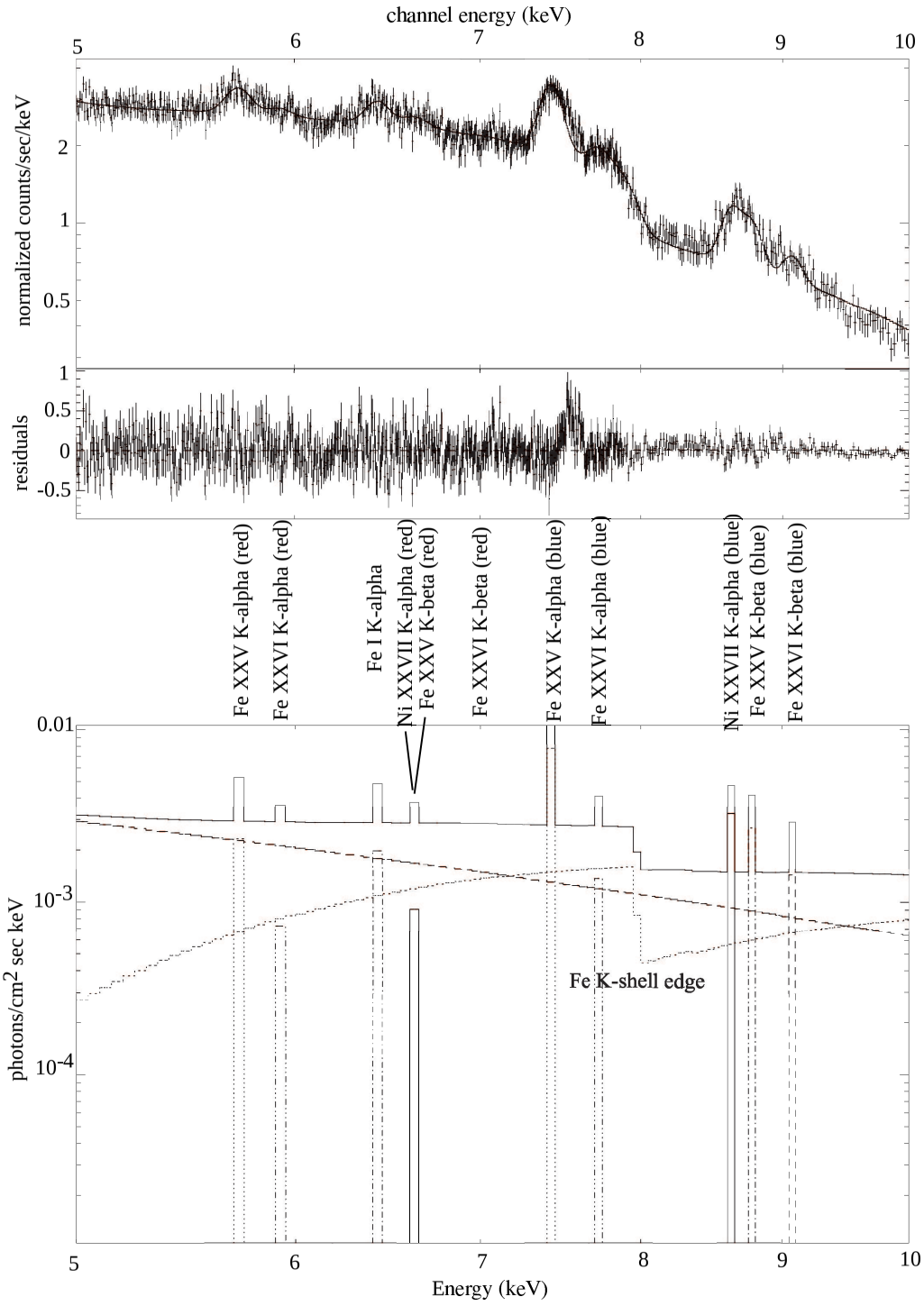

Figure 4.1: The XMM-Newton spectrum (top) and the best fit model (the solid line on top and bottom) on 2003 October 19 ($5.0-10$keV). The blended lines of Ni $_{\rm XXVII}$ Kα and Fe $_{\rm XXV}$ Kβ are resolved in spectral fitting. The emission line from Fe $_{\rm XXVI}$ Kβ from the red jet is not detected. The model shows Fe K-shell absorption edge.

Table 4.1: Results of the model fit to the spectrum of 2003 October 19. All uncertainties refer to statistical 90% confidence limits.

Parameter		
Fe K-shell absorption edge		
Edge energy	$7.956^{+0.044}_{-0.010}\,\mathrm{keV}$	
$N_{\mathrm{H\,lea}}$	$96.1^{+5.7}_{-3.0} \times 10^{22}\mathrm{cm}^{-2}$	
Bremsstrahlung		
kT	$8.38^{+0.20}_{-0.37}\,\mathrm{keV}$	
A_1 [a]	$5.08^{+0.08}_{-0.05} \times 10^{38}\,\mathrm{cm}^{-3}$	
A_2 [b]	$2.09^{+0.19}_{-0.19} \times 10^{39}\,\mathrm{cm}^{-3}$	
$0.5-10\,\mathrm{keV}$ Model Flux (absorbed)	$2.60 \times 10^{-10}\,\mathrm{ergs\,cm^{-2}\,s^{-1}}$	
$0.5-10\,\mathrm{keV}$ Model Flux (absorption-corrected)	$8.92 \times 10^{-10}\,\mathrm{ergs\,cm^{-2}\,s^{-1}}$	
Line Flux: $10^{-5}\,\mathrm{photon\,s^{-1}\,cm^{-2}}$ (rest-frame line energy)	Red	Blue
Fe $_{\mathrm{XXV}}$ Kα (6.698 keV)	$11.8^{+1.5}_{-1.3}$	$39.4^{+2.1}_{-1.7}$
Fe $_{\mathrm{XXVI}}$ Kα (6.965 keV)	$3.7^{+1.4}_{-1.2}$	$6.9^{+1.7}_{-1.6}$
Ni $_{\mathrm{XXVII}}$ Kα (7.798 keV)	$4.6^{+1.2}_{-1.7}$	$16.4^{+2.0}_{-1.4}$
Fe $_{\mathrm{XXV}}$ Kβ (7.897 keV)	< 1.7	$13.5^{+1.6}_{-1.7}$
Fe $_{\mathrm{XXVI}}$ Kβ (8.210 keV)	< 1.6	$7.2^{+1.7}_{-1.5}$
Fe $_{\mathrm{I}}$ Kα (6.399 keV)	$10.0^{+1.0}_{-2.0}$	
Redshift	$0.1728^{+0.0004}_{-0.0021}$	$-0.0976^{+0.0002}_{-0.0003}$
χ^2/d.o.f	861 / 740	

a): Emission measure of the thermal bremsstrahlung continuum defined by $\int n_{\mathrm{e}}\, n_{\mathrm{I}}\, \mathrm{dV}$, where n_{e},n_{I} are the electron and ion densities.

b): Emission measure of the thermal bremsstrahlung continuum attenuated by leaky absorber.

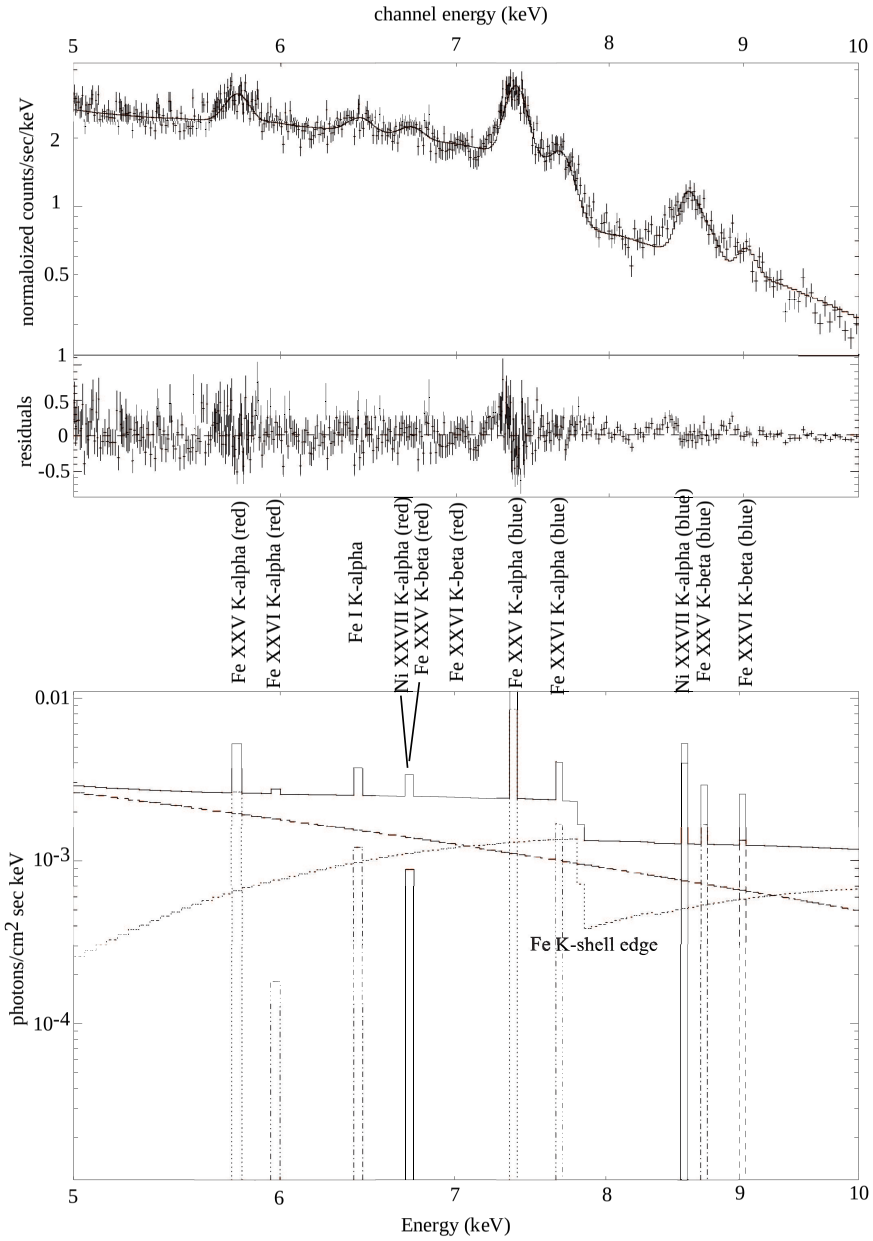

Figure 4.2: The XMM-Newton spectrum (top) and the best fit model (the solid line on top and bottom) of SS433 on 2003 October 25 ($5.0-10$keV). The blended lines of $\mathrm{Ni}_{\mathrm{XXVII}}\,\mathrm{K}\alpha$ and $\mathrm{Fe}_{\mathrm{XXV}}\,\mathrm{K}\beta$ are resolved in spectral fitting. The emission lines from $\mathrm{Fe}_{\mathrm{XXVI}}\,\mathrm{K}\alpha$ and $\mathrm{Fe}_{\mathrm{XXVI}}\,\mathrm{K}\beta$ from the red jet are not detected. The model shows Fe K-shell absorption edge.

Table 4.2: Results of the model fit to the spectrum of 2003 October 25. All uncertainties refer to statistical 90% confidence limits.

Parameter		
Fe K-shell absorption edge		
Edge energy	$7.800^{+0.057}_{-0.005}\,\mathrm{keV}$	
$N_{\mathrm{H\,lea}}$	$95.4^{+5.7}_{-4.9} \times 10^{22}\mathrm{cm}^{-2}$	
Bremsstrahlung		
kT	$6.80^{+0.20}_{-0.32}\,\mathrm{keV}$	
A_1 [a]	$5.02^{+0.178}_{-0.079} \times 10^{38}\,\mathrm{cm}^{-3}$	
A_2 [b]	$2.15^{+0.23}_{-0.45} \times 10^{39}\,\mathrm{cm}^{-3}$	
$0.5-10\,\mathrm{keV}$ Model Flux (absorbed)	$2.40 \times 10^{-10}\,\mathrm{ergs\,cm^{-2}\,s^{-1}}$	
$0.5-10\,\mathrm{keV}$ Model Flux (absorption-corrected)	$9.69 \times 10^{-10}\,\mathrm{ergs\,cm^{-2}\,s^{-1}}$	
Line Flux $10^{-5}\,\mathrm{photon\,s^{-1}\,cm^{-2}}$ (rest-frame line energy)	Red	Blue
$\mathrm{Fe\,_{XXV}\,K}\alpha$ $(6.698\,\mathrm{keV})$	$13.4^{+1.8}_{-1.7}$	$43.5^{+2.5}_{-2.3}$
$\mathrm{Fe\,_{XXVI}\,K}\alpha$ $(6.965\,\mathrm{keV})$	< 2.5	$8.5^{+1.9}_{-2.0}$
$\mathrm{Ni\,_{XXVII}\,K}\alpha\,(7.798\,\mathrm{keV})$	$4.5^{+1.8}_{-1.6}$	$20.2^{+2.2}_{-2.0}$
$\mathrm{Fe\,_{XXV}\,K}\beta$ $(7.897\,\mathrm{keV})$	< 1.6	$8.4^{+2.7}_{-1.4}$
$\mathrm{Fe\,_{XXVI}\,K}\beta$ $(8.210\,\mathrm{keV})$	< 820	$6.7^{+1.9}_{-1.9}$
$\mathrm{Fe\,_{I}\,K}\alpha$ $(6.399\,\mathrm{keV})$	$6.1^{+1.3}_{-2.1}$	
Redshift	$0.1622^{+0.0003}_{-0.0005}$	$-0.0923^{+0.0000}_{-0.0004}$
χ^2/d.o.f	552 / 430	

a): Emission measure of the thermal bremsstrahlung continuum defined by $\int n_{\mathrm{e}}\, n_{\mathrm{I}}\, \mathrm{dV}$, where n_{e},n_{I} are the electron and ion densities.

b): Emission measure of the thermal bremsstrahlung continuum attenuated by the leaky absorber.

of a higher temperature becomes in the observed flux, and thus higher best-fit temperature would be obtained. The band pass of the LAC detector of Ginga is $\leq 30\,\mathrm{keV}$, while that of the EPIC-pn of XMM-Newton is $0.15 - 15\,\mathrm{keV}$. Therefore, a temperature value determined from the LAC of Ginga data can be higher than that from the EPIC-pn of XMM-Newton.

From the ratio of A_1 to A_2, attenuating matter is consider to cover most of the X-ray jet.

Chapter 5

Discussion

In Figure 4.1 and 4.2, a shifted Fe K-shell absorption edge is shown. It has never been detected a edge like that. To detect the edge is one of the accomplishments of my thesis. The EPIC-pn ,which has very large effective area and good energy resolution around 5.0−10 keV, enable to detect the edge.

Two simple mechanism which explain the shift of the edge from the neutral value of 7.11 keV are proposed: 1. The Fe in the absorbing plasma is considerably ionized. 2. The attenuating matter is outflowing at a high velocity. In Table 5.1, the Fe ionization state and the plasma Doppler sift which was obtained from the edge energy is shown.

In this chapter I figure out the size and the electron density of the absorbing plasma along each interpretations and discuss the plasma geometry. In the following section,

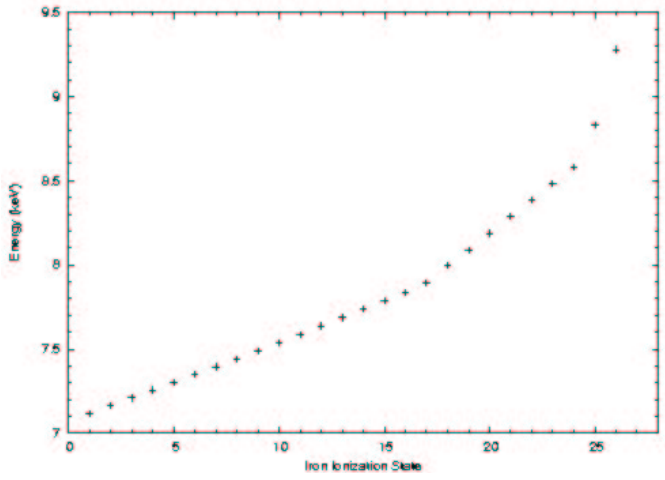

Figure 5.1: The relation between Fe ionization state and Fe K-shell edge energy (Lotz 1968, Makishima 1986).

Table 5.1: Interpretation of shifted absorption edge

	2003 October 19	2003 October 25
$E_{\rm edge}{}^a$ (keV)	$7.956^{+0.044}_{-0.010}$	$7.800^{+0.057}_{-0.005}$
ionization state^b	$\mathrm{Fe\,_{XVII}} - \mathrm{Fe\,_{XVIII}}$	$\mathrm{Fe\,_{XV}} - \mathrm{Fe\,_{XVI}}$
Doppler shift z	$-0.1055^{+0.0012}_{-0.0049}$	$-0.0876^{+0.0006}_{-0.0066}$

a): The iron K-shell absorption edge energy from spectral fitting.

b): Using data from Figure 5.1 (Lotz 1968).

firstly, I consider the case of ionized plasma in §5.1. Then, I consider the case of Doppler shifted plasma in §5.2.

5.1 Ionized plasma

Two mechanisms to ionize the Fe absorbing plasma are discussed. Collisional ionization and photoionization.

5.1.1 Collisional plasma model

I discuss on the model of a thermal absorbing plasma in collisional equilibrium in a spherical configuration with radius r. The absorption plasma absorbs the part of X-ray emission from the jets and radiate X-rays by collisional ionization.

The relation between plasma temperature and the population of each ion is given in Figure 5.2 (Jacobs *et al.* 1977). From the October 19 observation I get a corresponding temperature of $\mathrm{kT} = 0.27 - 0.43\,\mathrm{keV}$, from the October 25 $\mathrm{kT} = 0.17 - 0.22\,\mathrm{keV}$.

The luminosity of this thermal plasma in the XMM-Newton energy band $L_{\mathrm{col}\,0.5-10}$ is given as

$$L_{\mathrm{col}\,0.5-10} = \Lambda(T)\,\eta(T) \int n_{\mathrm{e}}\, n_{\mathrm{i}}\,\mathrm{dV}, \tag{5.1}$$

where $\Lambda(T)$ is the radiative cooling function, $\eta(T)$ is the ratio of the emission falling into the observable XMM-Newton energy band > 0.5keV to the total emission from the cloud (for details of the parameter $\eta(T)$ see Appendix A), n_{e} is the electron density, n_{i} is ion number density. The observed luminosity L_{obs} is the sum of $L_{\mathrm{col}\,0.5-10}$ and the luminosity of the absorbed jets. Therefore,

$$L_{\mathrm{col}\,0.5-10} < L_{\mathrm{obs}}. \tag{5.2}$$

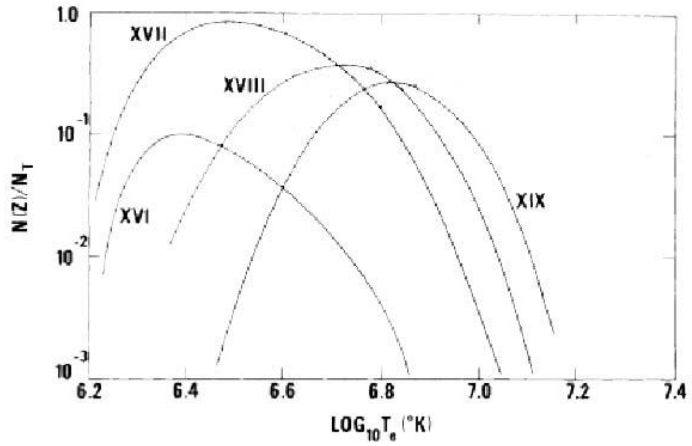

Figure 5.2: The ionization equilibrium for $\mathrm{Fe\,_{XVI}} - \mathrm{Fe\,_{XIX}}$ (Jacobs *et al.* 1977). The relation between plasma temperature and population of each ion is shown.

$L_{\rm obs}$ is given by $L_{\rm obs} = 4\pi d^2 f_{obs} (\simeq 7 \times 10^{35}\,{\rm erg\,s^{-1}})$, where d is the distance to SS433 and $f_{\rm obs}$ is the observed flux, for which the absorbed flux in Table 4.1 and Table 4.2. I assume that $n_{\rm e} \simeq n_{\rm i} \simeq \frac{N_{\rm H}}{r}$ and $\int n_{\rm e}\, n_{\rm i}\, {\rm dV} = \frac{4}{3}\pi {N_{\rm H}}^2\, r$, where $N_{\rm H}$ is the equivalent hydrogen column density of the attenuating plasma. Therefore, from equation (5.1) and equation (5.2), the radius is constrained as

$$r < \frac{3d^2\, f_{\rm obs}}{\Lambda(T)\, \eta(T)\, {N_{\rm H}}^2}. \tag{5.3}$$

In Figure 5.3(Gaetz and Salpeter 1983), the relation between the radiative cooling function $\Lambda(T)$ and the plasma temperature is plotted. From Figure 5.3 I find $\Lambda(0.43\,{\rm keV}) = 10^{-23.15}$ and $\Lambda(0.22\,{\rm keV}) = 10^{-23.90}$. From Appendix A, it is estimated $\eta(0.43\,{\rm keV}) = 0.32$ and $\eta(0.22\,{\rm keV}) = 0.10$. With the distance of SS433 $d = 4.85\,{\rm kpc}$ (Vermeulen *et al.* 1993), I get below from equation (5.3):

October 19

$$\begin{aligned} & r < 8.9 \times 10^{10}{\rm cm} \\ & n_{\rm e} > 1.0 \times 10^{13}{\rm cm^{-3}} \end{aligned} \tag{5.4}$$

October 25

$$\begin{aligned} & r < 1.6 \times 10^{12}{\rm cm} \\ & n_{\rm e} > 5.8 \times 10^{11}{\rm cm^{-3}}. \end{aligned} \tag{5.5}$$

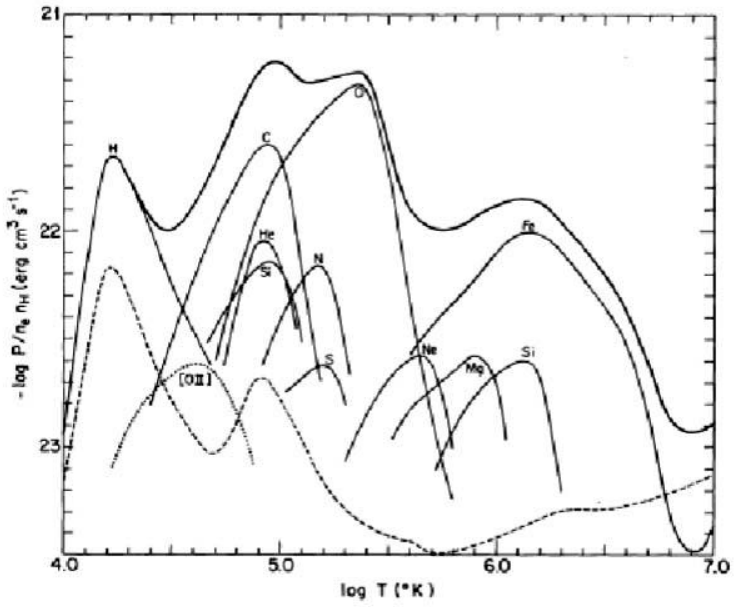

Figure 5.3: Radiative cooling function $\Lambda(T)$ for a gas in collisional equilibrium. Here $\Lambda(T)$ is denoted by $\mathrm{P/n_e\,n_H}$. Contributions to cooling from individual elements are indicated (Gaetz Salpeter 1983).

5.1.2 Photoionized plasma model

I discuss on the model of the photoionized absorbing plasma in a spherical configuration with radius r. The absorbing plasma absorb the part of the X-ray emission from the jets and is photoionized by the X-rays from the jets.

From Figure 5.4 (the model 4 in Kallman and McCray 1982), the ionization state can be converted to the ξ parameter: on October 19, it is $\xi = 10^{1.85} - 10^{2.00}$, on October 25, it is $\xi = 10^{1.65} - 10^{1.70}$. The ξ parameter is defined as $\xi = \frac{L_{\rm src}}{4\pi\, r^2\, n_{\rm e}}$, where $L_{\rm src}$ is the X-ray source luminosity and $n_{\rm e}$ is the electron density. I assume that the ξ parameter is constant in the absorbing plasma and $n_{\rm e} \simeq \frac{N_{\rm H}}{r}$, where $N_{\rm H}$ is the equivalent hydrogen column density from Table 4.1 and 4.2. I assume that $L_{\rm src} \simeq 4\pi\, d^2\, f_{\rm org} (\simeq 3 \times 10^{36}\,{\rm erg\,s^{-1}})$, where $f_{\rm org}$ is the absorption-corrected flux in Table 4.1 and 4.2 and d is the distance to SS433. Therefore,

$$r \simeq \frac{d^2\, f_{\rm org}}{N_{\rm H}\, \xi}, \tag{5.6}$$

which gives for $d = 4.85\,{\rm kpc}$ (as in §5.1.1),

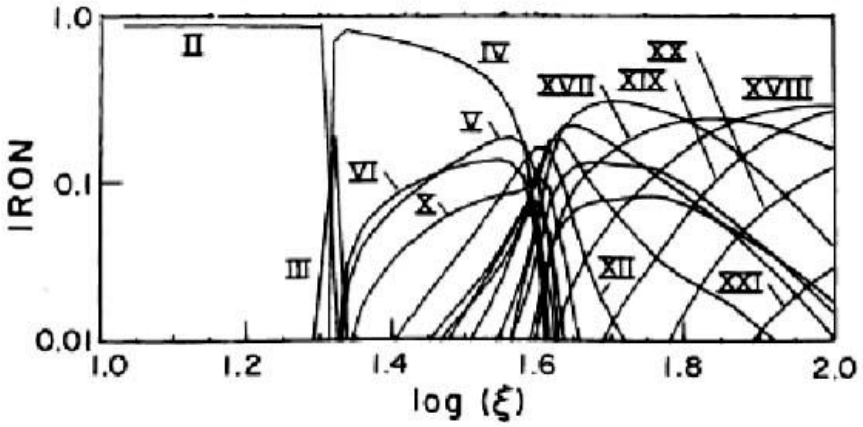

Figure 5.4: Fe ionization structure of model 4. Relative abundances of iron of each element is shown as a function ξ. This model is assumed the source luminosity is $L_{\rm src} = 10^{37}{\rm erg\,s^{-1}}$, gas density $n = 10^{11}{\rm cm^{-3}}$, and 10 keV bremsstrahlung+line trapping (Kallman and McCray 1982).

October 19

$$r \simeq 2.0 - 3.0 \times 10^{9}{\rm cm} \qquad (5.7)$$
$$n_{\rm e} \simeq 3.1 - 5.2 \times 10^{14}{\rm cm^{-3}}$$

October 25

$$r \simeq 4.3 - 5.4 \times 10^{9}{\rm cm} \qquad (5.8)$$
$$n_{\rm e} \simeq 1.7 - 2.4 \times 10^{14}{\rm cm^{-3}}.$$

5.1.3 The geometry

The absorbing plasma is in collisional equilibrium, the estimated size of the plasma is rather small. From the ratio of A_1 and A_2 (see Table 4.1 and Table 4.2), the length of the absorbed X-ray jet should be longer than the unabsorbed X-ray jet[1] . If the plasma is in collisional equilibrium, this difficulty is resolved by reducing the plasma temperature. This means that the plasma is ionized not only by collisions but also by photoionization. Therefore, the plasma in which collisional ionization is dominant is unlikely as the nature of the leaky attenuator and I consider only the case of photoionization.

If the plasma is photoionized, the estimated size of the plasma is rather small too and the simple spherical photoionized plasma model is rejected. If the leaky absorber is

[1] In this thesis, length of the X-ray jet is to be $\sim 10^{12}$ cm (Kotani 1998)

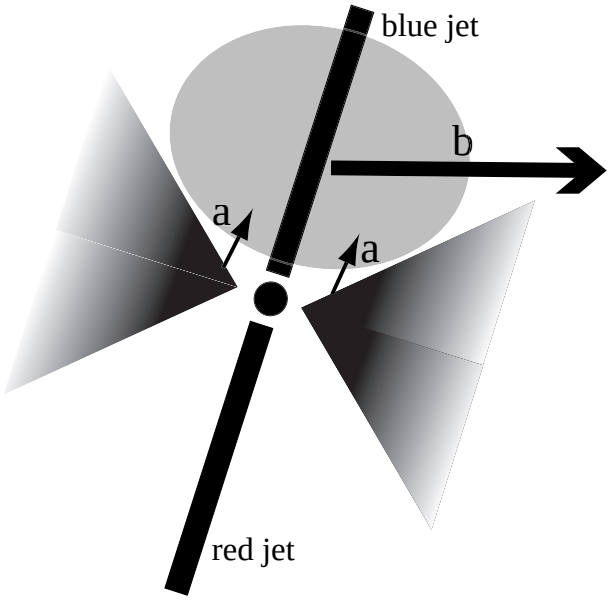

Figure 5.5: The improved geometry of the photoionized plasma. The center circle is the compact star and the two triangles represent the accretion disk and the gray ellipse is the absorbing plasma. The absorbing plasma is photoionized by X-rays from the inner part of the accretion disk (a). Radiation (b) is observed as absorbed emission from the jet.

photoionized, it would have a more complicated geometry.

I suggest a more realistic geometry as shown in Figure 5.5. It resolved the difficulty by "unobserved X-rays", because if $L_{\rm src}$ increases, r increases too. A candidate for the "unobserved X-rays" are emission from the inner accretion disk and the base of the jets which are hidden by the rim of the accretion disk. These X-rays photoionize the absorbing plasma but are not observed. If the size of the absorption plasma is $r \simeq 10^{12}\,{\rm cm}^{-3}$, as the same order as the X-ray jet, all of the X-ray luminosity of SS433 would be derived as $L_{\rm src} \simeq 10^{39}\,{\rm erg\,s}^{-1}$ from equation (5.6).

In this case, the width of the emission lines would be expanded by comptonization, because the optical depth of the absorbing plasma $\tau \sim 1$ ($\tau = \sigma_T \times N_{\rm H}$, where σ_T is the cross section of Thomson scattering). The relation between ξ parameter and plasma temperature is shown in Figure 5.6 (model 4 in Kallman and McCray 1982) and line hair-width as function of optical depth and plasma temperature for the line on 6.41 keV are shown in Figure 5.7 (Pozdnyakov *et al.* 1979). From Figure 5.6 temperature of the absorbing plasma is estimated as $kT \sim 1\,{\rm eV}$. Therefore, from Figure 5.7, the half-width of the emission lines would be $\Delta_{1/2}\,h\nu \sim 0.1\,{\rm keV}$. At Fe XXV K$\alpha$ lines from the blue jet in Figure 4.1 and 4.2, the observed line width is wider than model line width, which may be

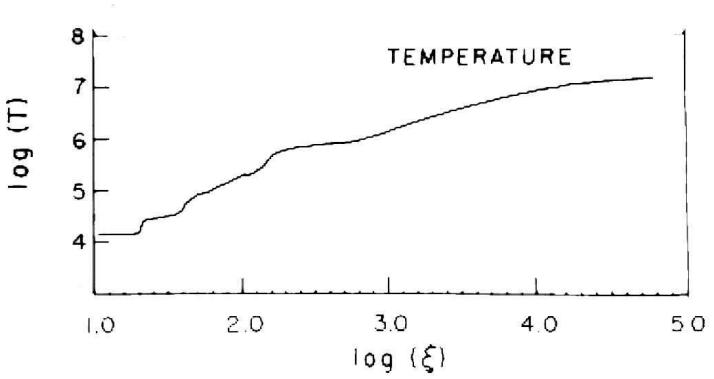

Figure 5.6: The ξ parameter versus the plasma temperature of model 4 (Kallman *et al.* 1982). This model is assumed the source luminosity is $L_{\rm src} = 10^{37}{\rm erg\,s^{-1}}$, gas density $n = 10^{11}{\rm cm^{-3}}$, and 10 keV bremsstrahlung+line trapping.

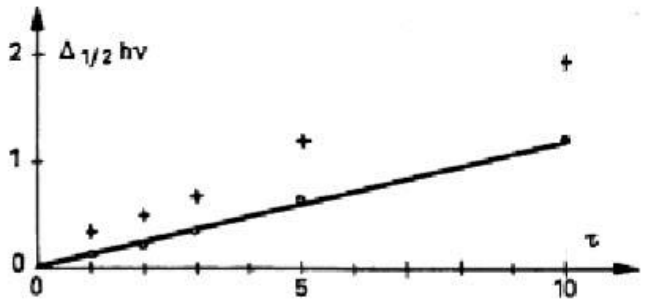

Figure 5.7: Emission line half-width $\Delta_{1/2}\, h\nu\,({\rm keV})$,which pass through plasma and due to comptonization, as function of optical depth τ and plasma temperature $kT_{\rm e}\,({\rm keV})$ for the line $h\nu_0 = 6.41\,{\rm keV}$ (Pozdnyakov *et al.* 1979). This is results of Monte Carlo Computations. The *cross* points are $kT_{\rm e} = 1\,{\rm keV}$ and the *circle* points are $kT_{\rm e} = 0\,{\rm keV}$.

accounted with the Compton broadening effect.

If this model gives a good explanation for the source, the absorption edge energy will be not vary with precession phase.

5.2 Doppler shifted plasma

In this section, I discuss on the possibility of an absorbing matter moving along the jets. The Doppler shifts of the blue jet and the moving absorbing matter are compared in Table 5.2. The absorbing matter including not or low ionized Fe atoms is assumed to be moving

Table 5.2: Doppler shifts of the blue jet and the moving absorbing plasma

	2003 October 19	2003 October 25
Observed Doppler shift of the blue jet $z_{\rm blue}$	$-0.0976^{+0.0002}_{-0.0003}$	$-0.0923^{+0.0000}_{-0.0004}$
Doppler shift of the moving absorbing matter $z_{\rm edge}$	$-0.1055^{+0.0012}_{-0.0049}$	$-0.0876^{+0.0006}_{-0.0066}$

at the same velocity of the blue jet.

An interpretation of the moving absorber is that is inhomogeneous, as schematically drawn in Figure 5.9. The jets and the plasma are assumed to be in a pressure equilibrium, *i.e.*,

$$n_j \cdot T_j = n \cdot T, \tag{5.9}$$

where n is the plasma density and T is the temperature. The subscript "$_j$" denotes the value of the jet. Since the jet is expanding, $n_j < n_0$ and $T_j < T_0$ where the subscript "0" denotes the value of the base of the jets. Substituting the typical jet parameters ,$n_0 \simeq 10^{13}\,{\rm cm}^{-3}$, $T_0 \simeq 10^8\,{\rm K}$, and a temperature at which Fe is not ionized, $T \simeq 10^4\,{\rm K}$ (see Figure 5.2), I obtain $n > 10^{17}\,{\rm cm}^{-3}$. I assume that $n \simeq n_{\rm e} \simeq \frac{N_{\rm HIea}}{r}$, where $n_{\rm e}$ is the electron density and r is the characteristic scale of the absorbing matter. Therefore, it is constrained as $r < 10^7\,{\rm cm}$, which is smaller than the radius of the jet at the base, $r_0 > 3 \times 10^9\,{\rm cm}$.

I suggest a model of the many moving matter in the jet because the major part of the X-ray emission are absorbed. If the 100 moving matter in the jet[2] , the ξ parameter of the matter would be $\xi \sim 10$, which is consistent with the low ionized hypothesis.

Origin of the inhomogeneous jet may be explained by low ionized dense blobs around the jets absorb the X-ray emission from the jets. Brinkmann *et al.* (1998) suggest the possible formation of dense blobs by a thermal instability. However to consider this possibility is out of this thesis.

If the moving attenuator model is valid, the Doppler shift of the absorption edge would vary in accordance with the precession of the jets. The model will be confirmed or denied in future observations of XMM-Newton at a different phase.

[2] The typical X-ray jet's length divided by ten times estimated radius of the moving matter.

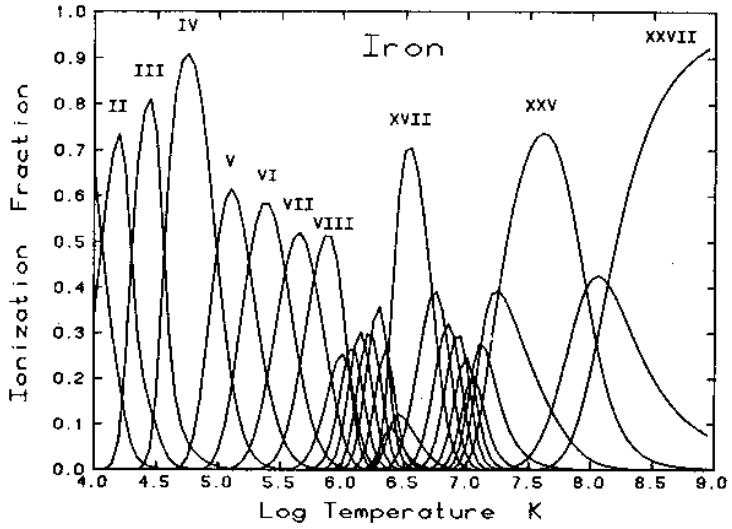

Figure 5.8: Collisional equilibrium model fractional abundances of ionization stages of iron (McCray 1987, Shull and Van Steenberg 1982).

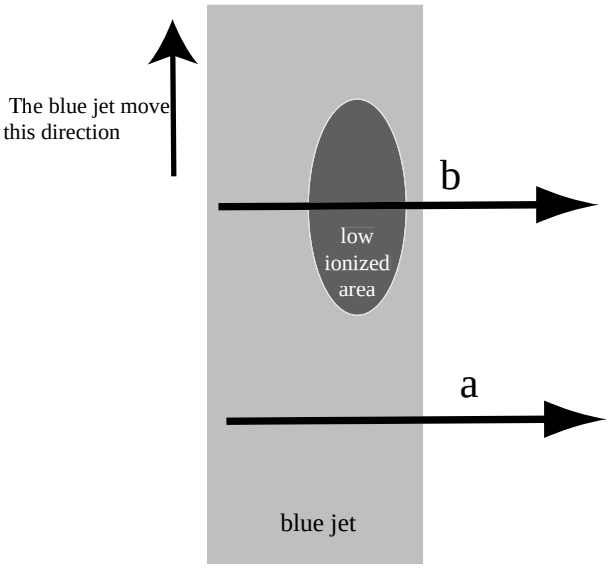

Figure 5.9: A schematic view of an inhomogeneous jet. X ray (a) is observed as unabsorbed. X ray (b) is observed as absorbed by low ionization plasma.

Chapter 6

Conclusion

In this thesis, the observation data of microquasar SS433 taken with the pn camera of the European Photon Imaging Camera onboard XMM-Newton on 2003 October 18 and on 2003 October 25 are analyzed. One of the principle investigator of the observation is W.Brinkmann. A Fe K-shell absorption edge with an energy different from that of neutral atom at rest frame is detected in the 5.0−10 keV range spectra thanks to the high sensitivity of the instrument.

The results of this thesis are summarized as follows.

- The shifted Fe K-shell edge at $E = 7.956^{+0.044}_{-0.010}\,\mathrm{keV}$, with a column density of $N_{\mathrm{H}} = 96.1^{+5.7}_{-3.0} \times 10^{22}\,\mathrm{cm}^{-2}$ in October 19 and at $E = 7.800^{+0.057}_{-0.005}\,\mathrm{keV}$ $N_{\mathrm{H}} = 95.4^{+5.7}_{-4.9} \times 10^{22}\,\mathrm{cm}^{-2}$ in October 25 are detected. Two simple mechanisms to explain the edge energy shift are proposed: 1. The iron in the absorbing plasma is considerably ionized as $\mathrm{Fe\,_{XV}} - \mathrm{Fe\,_{XVIII}}$. 2. The attenuating matter is moving along the blue jet.

- The iron absorbing plasma is assumed to be ionized, whether the ionizing mechanism are collisional ionization or photoionization, the estimated size of the absorbing plasma r would become too short ($r \simeq 10^9\,\mathrm{cm}$) compared with the jet length of 10^{12} cm. This problem is resolved by postulating additional "unobserved X-rays". A strong candidate for "unobserved X-rays" are emission from the inner accretion disk and the base of the jets.

- If the absorbing matter moves at the velocity of the blue jet, the assumption that the jets have an inhomogeneous internal structure and that dense blobs exist around the jets may give a good explanation.

I favor the "unobserved X-rays" hypothesis more to the other hypotheses because it's simplicity, but I can not reject the others. The analysis of the observations at other precessional phases may give more insight.

Appendix A

An estimate of parameter $\eta(T)$

Parameter $\eta(T)$ is the ratio of the emission falling into the observable XMM-Newton energy band 0.5−15 keV (it is shown in §5.1.1). In this appendix, I describe how to estimate $\eta(T)$.

Thermal bremsstrahlung emission ε_ν^{ff} (erg s^{-1} cm^{-3} Hz^{-1}) is figured by

$$\varepsilon_\nu^{ff} = 6.8 \times 10^{-38}\, Z^2\, n_{\rm e}\, n_{\rm i}\, T^{-\frac{1}{2}}\, e^{-\frac{h\nu}{kT}}\, \bar{g}_{ff}, \tag{A.1}$$

where Z is an atomic number, $n_{\rm e}$ is a electron density, , $n_{\rm i}$ is a ion density, T is a plasma temperature, h is the Planck's constant, ν is a frequency of the wave of light, k is the Boltzmann's constant, and $\bar{g}_{ff}$ is a velocity averaged gaunt factor (Rybicki and Lightman 1979). Therefore,the ratio of the emission fall into 0.5−10 keV is

$$\eta(T) = \frac{\int_{0.5\,{\rm keV}}^{10\,{\rm keV}} e^{-\frac{h\nu}{kT}}\, \bar{g}_{ff}\, d\nu}{\int_{0\,{\rm keV}}^{\infty} e^{-\frac{h\nu}{kT}}\, \bar{g}_{ff}\, d\nu}. \tag{A.2}$$

In Figure A.1, the gaunt factor $\bar{g}_{ff}$ for thermal bremsstrahlung is shown. In the case of §5.1.1, plasma temperature kT=0.43 keV or kT=0.22 keV, and one of the main plasma components is Fe ion, then $\frac{h\nu}{kT} > 1$ and $\frac{kT}{Z^2\, Ry}$, where Ry=13.6 eV. Therefore, from Figure A.1, $\bar{g}_{ff} \simeq 1$. Furthermore, the emission from this temperature plasma falling into the 0.5−15 keV is almost same as the emission falling into the 0.5−∞ keV, because the emission in this temperature plasma falling into over 15 keV is very small. Therefore, Equation A.2 is rewrote as

$$\eta(T) \simeq \frac{\int_{0.5\,{\rm keV}}^{\infty} e^{-\frac{h\nu}{kT}}\, d\nu}{\int_{0\,{\rm keV}}^{\infty} e^{-\frac{h\nu}{kT}}\, d\nu} = e^{-\frac{0.5\,{\rm keV}}{kT}}. \tag{A.3}$$

Then, η(0.43 keV)=0.32 and η(0.22)=0.10 are obtained.

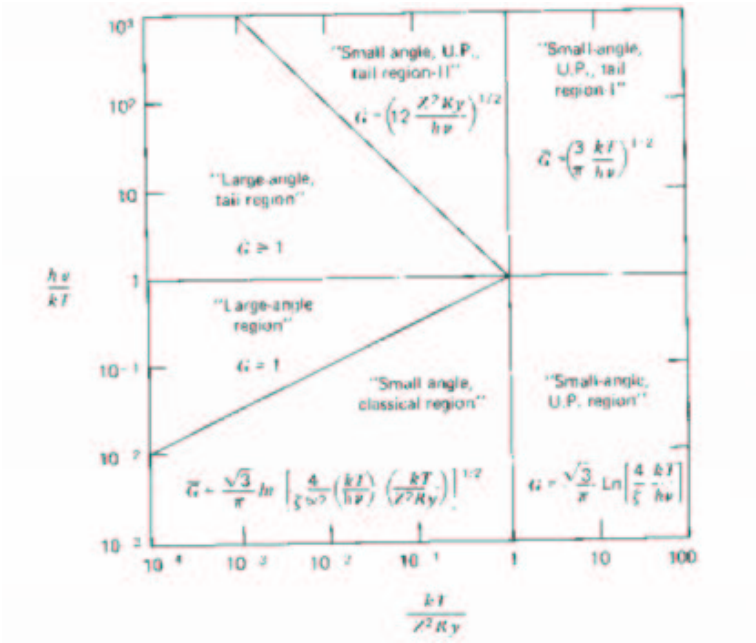

Figure A.1: Approximate analytic formula for the Gaunt factor $\bar{g}_{ff}(\nu, T)$ for thermal bremsstrahlung. Here $\bar{g}_{ff}$ is denoted by $\bar{G}$ and the energy unit Ry=13.6 eV (Rybicki and Lightman 1979, Novikov *et al.* 1973).

Bibliography

[1] Arnaud, K., Dorman, B., 2003, *XSPEC* An X-Ray Spectral Fitting Package Users' Guide,
http : *//xspec.gsfc.nasa.gov/docs/xanadu/xspec/manual/manual.html*

[2] Brinkmann, W., Fink, H. H., Massaglia, S., Bodo, G., Ferrari, A., 1988, A&A, **196**, 313

[3] Brinkmann, W., Kawai, N., Fink, H. H., 1991, A&A, **241**, 112

[4] Brinkmann, W., Aschenbach, B., Kawai, N., 1996, A&A, **312**, 306

[5] Brinkmann, W., Kotani, T., Kawai, N., 2005, A&A, **431**, 575

[6] Dubner, G. M., Holdaway, M., Goss, W. M., Mirable, I. F., 1998, Astron. J., **116**, 1842

[7] Ehle, M., Breitfellner, M., Riestra R. G., Guainazzi, M., Rodriguez, P., Santos-Lleo, M., Schartel, N., Tomas, L., Verdugo, E., Dahlem, M., 2004, XMM-Newton Users' Handbook,
http : *//xmm.vilspa.esa.es/xmm_user_support/*
external/documentation/uhb_frame.shtml

[8] Gaetz, T. J., Salpeter, E. E., 1983, ApJS, **52**, 155

[9] Glagyshev, S. A., Goranskii, V. P., Cherepashchuk, A. M., 1987, Sov. Astron., **31**, 541

[10] Goranskii, V. P., Esipov, V. F., Cherepashchuk, A. M., 1998, Astron. Reports, **42**, 209

[11] Jacob, V. L., Davis, J., Kepple, P. C., Blaha, M., 1977, ApJ, **211**, 605

[12] Kallman, T. R., McCray, R., 1982, ApJS, **50**, 263

[13] Kawai, N., Matsuoka, M., Pan, H. C., Stewart, G. C., 1989, PASJ, **41**, 491

[14] Kotani, T., Kawai, K., Aoki, T., John, D., Matuoka, M., Mitsuda, K., Nagase, F., Ricker, G., White, N. E., 1994, PASJ, **46**, 147

[15] Kotani, T., Kawai, N., Matsuoka, M., 1996, PASJ, **48**, 619

[16] Kotani, T., 1998, Doctral Thesis, University of Tokyo

[17] Loiseau.N, Ehle, M., Pollock, A. M. T., Talavera, C., Gabriel, B., Chen, B., Ballet, J., Dennerl, K., Freyberg, M., Guainazzi, M., Kirsch., M., Metcalfe, L., Osborne, J., Pietsch, W., Saxton, R., Smith, M., Verdugo, E., 2004, User's Guide to the XMM-Newton Science Analysis System,
http : *//xmm.vilspa.esa.es/external/xmm_user_support/*
*documentation/sas_usg*_3.0/*USG/index.html*

[18] Lotz, W., 1968, J. Opt. Soc. America, **58**, 915

[19] Makishima, K., 1986, in The Physics of Accretion onto Compact Objects, ed. Mason, K. O., Watson, M. G., White, N. E., (Springer: Germany), 249

[20] Margon, B., Holland, C. F., Jonathan, I. K., Karen, B. K., 1979a, ApJ, **230**, 41

[21] Margon, B., Holland, C. F., Steven, A. G., 1979b, ApJ, **233**, 63

[22] Margon, B., 1984, Annu. Rev. Astron. Astrophys., **22**, 507

[23] Margon, B., Anderson, S. F., 1989, ApJ, **347**, 448

[24] Marshall, H. L., Canizares, C. R., Schulz, N. S., 2002, ApJ, **564**, 941

[25] McCray, R., 1987, Spectroscopy of astrophisical plasma, ed. Dalgarno, A., Layzer, D., (Cambridge University Press: UK), 255

[26] Mirabel, I. F., Rodríguez, L. F., 1999, Annu. Rev. Astron. Astrophys., **37**, 409

[27] Namiki, M., Kawai, N., Kotani, K., Makishima, K., 2003, PASJ, **55**, 281

[28] Novikov, I. D., Thorne, K. S., 1973, in Black Holes, Les Houches, ed. DeWitt, C., DeWitt, B., (Gordon and Breach: USA)

[29] Pozdnyakov, L. A., Sobol, I. M., Sunyaev, R. A., 1979, A&A, **75**, 214

[30] Rybicki, G. B., Lightman, A. P., 1979, Radiative Processes in Astrophysics, (A Wiley-Interscience publication: USA), 155

[31] Safi-Harb, S., Ögelman, H., 1997, ApJ, **483**, 868

[32] Seaquist, E. R., Gregory, P. C., Crane, P. C., 1978, IAUC, **3256**, 2

[33] Shull, J. M., Van Steenberg, M., 1982, ApJS, **48**, 95

[34] Stephenson, C. B., Sanduleak, N., 1977, ApJS, **33**, 459

[35] Strüder, L., Briel, U., Dennerl, K., Hartmann, R., Kendziorra, E., Meidinger, N., Pfeffermann, E., Reppin, C., Aschenbach, B., Bornemann, W., Bräuninger, H., Burkert, W., Elender, M., Freyberg, M., Haberl, F., Hartner, G., Heuschmann, F., Hippmann, H., Kastelic, E., Kemmer, S., Kettenring, G., Kink, W., Krause, N., Müller, S., Oppitz, A., Pietsch, W., Popp, M., Predehl, P., Read, A., Stephan, K. H., Stötter, D., Trümper, J., Holl, P., Kemmer, J., Soltau, H., Stötter, R., Weber, U., Weichert, U., von Zanthier, C., Carathanassis, D., Lutz, G., Richter, R. H., Solc, P., Böttcher, H., Kuster, M., Staubert, R., Abbey, A., Holland, A., Turner, M., Balasini, M., Bignami, G. F., La Palombara, N., Villa, G., Buttler, W., Gianini, F., Lainé, R., Lumb, D., Dhez, P., 2001, A&A, **365**, 18

[36] Vermeulen R. C., Schilizzi, R. T., Spencer, R. E., Romney, J.D., Fejes, I., 1993, A&A, **270**, 177

[37] Watson, M. G., Stewart, G.C., Brinkmann, W., King, A. R., 1986, MNRAS, **222**, 261

[38] Yuan, W., Kawai, N., Brinkmann, W., Matsuoka, M., 1995, A&A, **297**, 451

[39] 福江純, 1993, 現代天文学演習 新・宇宙を解く, 横尾武夫 編, (恒星社: 日本), 148

Acknowledgments

This thesis would not have been completed without a lot of helps by many people. I would like to thank Prof. N. Kawai who allowed me to analyze the data of interesting system of SS433, taught me astrophysics, and gave me a lot of help. I also would like to thank Dr. T. Kotani who taught me how to analyze and interpret the data and how to write English, and answered number of my questions.

I wish to express my gratitude to Prof. W. Brinkmann who gave me the XMM-Newton's observation data used in this thesis, gave me a lot of meaningful advice, and checked my English.

I would like to thank Dr. J. Kataoka who taught me some basic astrophysics in a B4 seminar, Ms. R. Sato and Mr. Y. Yatsu who taught me how to use XSPEC, Mr. Y. Serino who taught me how to use Linux, and all of the member of Kawai and Watanabe laboratory!